University of Hertfordshire UH

Research Archive

Citation for published version:

Qing-Hua Tan, et al, 'The MALATANG Survey: The L_{GAS}–L_{IR} Correlation on Sub-kiloparsec Scale in Six Nearby Star-forming Galaxies as Traced by HCN $J = 4 \to 3$ and HCO$^+$ $J = 4 \to 3$', *The Astrophysical Journal,* Vol. 860(2): 165, June 2018.

DOI:

Document Version:

This is the Accepted Manuscript version.
The version in the University of Hertfordshire Research Archive may differ from the final published version.

Copyright and Reuse:

Enquiries

If you believe this document infringes copyright, please contact Research & Scholarly Communications at rsc@herts.ac.uk

The MALATANG Survey: the $L_{\rm gas} - L_{\rm IR}$ correlation on sub-kiloparsec scale in six nearby star-forming galaxies as traced by HCN $J = 4 \to 3$ and HCO$^+$ $J = 4 \to 3$

Qing-Hua Tan,[1] Yu Gao,[1] Zhi-Yu Zhang,[2,3] Thomas R. Greve,[4] Xue-Jian Jiang,[1] Christine D. Wilson,[5] Chen-Tao Yang,[1,6,7] Ashley Bemis,[5] Aeree Chung,[8] Satoki Matsushita,[9] Yong Shi,[10] Yi-Ping Ao,[11,1] Elias Brinks,[12] Malcolm J. Currie,[13] Timothy A. Davis,[14] Richard de Grijs,[15,16,17] Luis C. Ho,[15] Masatoshi Imanishi,[11] Kotaro Kohno,[18,19] Bumhyun Lee,[8] Harriet Parsons,[20] Mark G. Rawlings,[20] Dimitra Rigopoulou,[21] Erik Rosolowsky,[22] Joanna Bulger,[23,24] Hao Chen,[10] Scott C. Chapman,[25] David Eden,[26] Walter K. Gear,[27] Qiu-Sheng Gu,[10] Jin-Hua He,[28,29] Qian Jiao,[1] Dai-Zhong Liu,[30,1] Li-Jie Liu,[21,1] Xiao-Hu Li,[31] Michał J. Michałowski,[32] Quang Nguyen-Luong,[33,34,35] Jian-Jie Qiu,[10] Matthew W. L. Smith,[14] Giulio Violino,[12] Jian-Fa Wang,[1] Jun-Feng Wang,[36] Jun-Zhi Wang,[37] Sherry Yeh,[23,38] Ying-He Zhao,[39] and Ming Zhu[31]

[1] *Purple Mountain Observatory & Key Laboratory for Radio Astronomy, Chinese Academy of Sciences, 8 Yuanhua Road, Nanjing 210034, China*

[2] *Institute for Astronomy, University of Edinburgh, Royal Observatory, Blackford Hill, Edinburgh EH9 3HJ, UK*

[3] *ESO, Karl-Schwarzschild-Str.2, D-85748 Garching, Germany*

[4] *Department of Physics and Astronomy, University College London, Gower Street, London WC1E6BT, UK*

[5] *Department of Physics and Astronomy, McMaster University, Hamilton, Ontario L8S 4M1, Canada*

[6] *Institut d'Astrophysique Spatiale, CNRS, Univ. Paris-Sud, Université Paris-Saclay, Bât. 121, 91405, Orsay Cedex, France*

[7] *European Southern Observatory, Alonso de Córdova 3107, Casilla 19001, Vitacura, Santiago, Chile*

[8] *Department of Astronomy, Yonsei University, 50 Yonsei-ro, Seodaemun-gu, Seoul 03722, Korea*

[9] *Academia Sinica Institute of Astronomy and Astrophysics, P.O. Box 23-141, Taipei 10617, Taiwan*

[10] *School of Astronomy and Space Science, Nanjing University, Nanjing 210093, China*

[11] *National Astronomical Observatory of Japan, 2-21-1 Osawa, Mitaka, Tokyo 181-8588, Japan*

[12] *Centre for Astrophysics Research, University of Hertfordshire, College Lane, Hatfield AL10 9AB, UK*

[13] *RAL Space, Rutherford Appleton Laboratory, Harwell Campus, Didcot, Oxfordshire, OX11 0QX, United Kingdom*

[14] *School of Physics and Astronomy, Cardiff University, Queen's Buildings, The Parade, Cardiff CF24 3AA, UK*

[15] *Kavli Institute for Astronomy & Astrophysics and Department of Astronomy, Peking University, Yi He Yuan Lu 5, Hai Dian District, Beijing 100871, China*

[16] *Department of Physics and Astronomy, Macquarie University, Balaclava Road, North Ryde, NSW 2109, Australia*

[17] *International Space Science Institute–Beijing, 1 Nanertiao, Zhongguancun, Hai Dian District, Beijing 100190, China*

[18] *Institute of Astronomy, Graduate School of Science, The University of Tokyo, Osawa, Mitaka, Tokyo 181-0015, Japan*

[19] *Research Center for the Early Universe, Graduate School of Science, The University of Tokyo, 7-3-1 Hongo, Bunkyo-ku, Tokyo 113-0033, Japan*

[20] *East Asian Observatory, 660 N. A'ohōkū Place, University Park, Hilo, Hawaii 96720-2700, USA*

[21] *Department of Physics, University of Oxford, Oxford, OX1 3RH, UK*

[22] *University of Alberta, 116 St & 85 Ave, Edmonton, AB T6G 2R3, Canada*

[23] *Subaru Telescope, NAOJ, 650 N. A'ohōkū Place, Hilo, HI 96720, USA*

[24] *Institute for Astronomy Maui, University of Hawaii, 34 Ohia Ku St., Pukalani, HI, 96768, USA*

[25] *Department of Physics and Atmospheric Science, Dalhousie University, Halifax, NS B3H 4R2, Canada*

[26] *Astrophysics Research Institute, Liverpool John Moores University, IC2, Liverpool Science Park, 146 Brownlow Hill, Liverpool, L3 5RF, UK*

[27] *College of Physical Sciences and Engineering, Cardiff University, Cardiff CF24 3AA, UK*

[28] *Key Laboratory for the Structure and Evolution of Celestial Objects, Yunnan Observatories, Chinese Academy of Sciences, 396 Yangfangwang, Guandu District, Kunming, 650216, China*

[29] *Chinese Academy of Sciences South America Center for Astronomy, China-Chile Joint Center for Astronomy, Camino El Observatorio #1515, Las Condes, Santiago, Chile*

[30] *Max Planck Institute for Astronomy, Königstuhl 17, D-69117 Heidelberg, Germany*

[31] *National Astronomical Observatories, Chinese Academy of Sciences, Beijing 100012, China*

[32] *Astronomical Observatory Institute, Faculty of Physics, Adam Mickiewicz University, ul. Słoneczna 36, 60-286 Poznań, Poland*

[33] *NAOJ Chile Observatory, National Astronomical Observatory of Japan, 2-21-1 Osawa, Mitaka, Tokyo 181-8588, Japan*

Corresponding author: Qing-Hua Tan

qhtan@pmo.ac.cn

[34] *Korea Astronomy and Space Science Institute, 776 Daedeok daero, Yuseoung, Daejeon 34055, Korea*
[35] *CITA, University of Toronto, 60 St. George Street, Toronto, ON M5S 3H8, Canada*
[36] *Department of Astronomy, Xiamen University, 422 Siming South Road, Xiamen 361005, China*
[37] *Shanghai Astronomical Observatory, Chinese Academy of Sciences, 80 Nandan Road, Shanghai 200030, China*
[38] *W. M. Keck Observatory, 65-1120 Mamalahoa Hwy, Kamuela, HI 96743, USA*
[39] *Yunnan Observatories, Chinese Academy of Sciences, Kunming 650011, China*

ABSTRACT

We present HCN $J = 4 \to 3$ and HCO$^+$ $J = 4 \to 3$ maps of six nearby star-forming galaxies, NGC 253, NGC 1068, IC 342, M82, M83, and NGC 6946, obtained with the James Clerk Maxwell Telescope as part of the MALATANG survey. All galaxies were mapped in the central $2' \times 2'$ region at $14''$ (FWHM) resolution (corresponding to linear scales of $\sim 0.2 - 1.0$ kpc). The $L_{\rm IR} - L'_{\rm dense}$ relation, where the dense gas is traced by the HCN $J = 4 \to 3$ and the HCO$^+$ $J = 4 \to 3$ emission, measured in our sample of spatially-resolved galaxies is found to follow the linear correlation established globally in galaxies within the scatter. We find that the luminosity ratio, $L_{\rm IR}/L'_{\rm dense}$, shows systematic variations with $L_{\rm IR}$ within individual spatially resolved galaxies, whereas the galaxy-integrated ratios vary little. A rising trend is also found between $L_{\rm IR}/L'_{\rm dense}$ ratio and the warm-dust temperature gauged by the 70 μm/100 μm flux ratio. We find the luminosity ratios of IR/HCN(4-3) and IR/HCO$^+$(4-3), which can be taken as a proxy for the efficiency of star formation in the dense molecular gas (SFE$_{\rm dense}$), appears to be nearly independent of the dense-gas fraction ($f_{\rm dense}$) for our sample of galaxies. The SFE of the total molecular gas (SFE$_{\rm mol}$) is found to increase substantially with $f_{\rm dense}$ when combining our data with that on local (ultra)luminous infrared galaxies and high-z quasars. The mean $L'_{\rm HCN(4-3)}/L'_{\rm HCO^+(4-3)}$ line ratio measured for the six targeted galaxies is 0.9±0.6. No significant correlation is found for the $L'_{\rm HCN(4-3)}/L'_{\rm HCO^+(4-3)}$ ratio with the SFR as traced by $L_{\rm IR}$, nor with the warm-dust temperature, for the different populations of galaxies.

Keywords: galaxies: ISM — galaxies: star formation — infrared: galaxies — ISM: molecules — radio lines: galaxies

1. INTRODUCTION

In the last two decades we have seen significant advances in our understanding of the relationship between star formation and the interstellar gas, from which stars form, in large part thanks to galaxy surveys at (sub)millimeter bands of multiple molecular species (e.g., Kennicutt 1998; Gao & Solomon 2004a,b; Bigiel et al. 2008; Leroy et al. 2008; Baan et al. 2008; Graciá-Carpio et al. 2008; Daddi et al. 2010; Shi et al. 2011, 2018; García-Burillo et al. 2012; Zhang et al. 2014; Greve et al. 2014; Lu et al. 2014; Usero et al. 2015). It has become clear that the molecular gas, rather than the atomic gas, is the raw material for star formation. The Kennicutt-Schmidt (K-S) law that relates the global surface densities of star-formation rate (SFR) and that of total gas including atomic and molecular gas (traced by H I 21 cm line and rotational lines of CO, respectively), is characterized by a power-law index of $n \approx 1.4$ ($\Sigma_{\rm SFR} \propto \Sigma_{\rm gas}^n$) (see Kennicutt 1998; Kennicutt & Evans 2012, and reference therein). The super linear slope derived in this empirical scaling relation suggests that the star-formation efficiency (SFE) indicated by the SFR per unit mass of molecular gas increases with SFR.

Bigiel et al. (2008) examined the resolved K-S law on sub-kpc scale (~ 750 pc) in nearby spiral and dwarf galaxies, and did not find significant correlation between $\Sigma_{\rm HI}$ and $\Sigma_{\rm SFR}$, as the H I surface density is shown to saturate at about 9 $M_\odot$ pc^{-2}. In contrast, a slope of unity relates $\Sigma_{\rm SFR}$ and $\Sigma_{\rm H_2}$ for normal and dwarf galaxies (Schruba 2013). However, the slope steepens for the $\Sigma_{\rm SFR} - \Sigma_{\rm H_2}$ relation if we expand the sample to include galaxies with extreme starbursts, such as luminous infrared galaxies (LIRGs, $10^{11}L_\odot \leqslant L_{\rm IR} < 10^{12}L_\odot$) and ultraluminous infrared galaxies (ULIRGs, $L_{\rm IR} \geqslant 10^{12}L_\odot$), which is evident both from observations (e.g., Gao & Solomon 2004a; Daddi et al. 2010; Liu et al. 2015b) and theoretical predictions (e.g., Krumholz & McKee 2005; Elmegreen 2015, 2018). In addition, a breakdown of the K-S law is found at giant molecular cloud (GMC) scales of a few tens of pc (e.g., Onodera et al. 2010; Nguyen-Luong et al. 2016), which is attributed to the dynamical evolution of GMCs and the drift of young clusters from their GMCs.

A large HCN $J = 1 \rightarrow 0$ survey in nearby spiral galaxies and (U)LIRGs performed by Gao & Solomon (2004a,b) revealed a tight linear correlation between the infrared (IR) and the HCN luminosities for normal star-forming galaxies and starbursts. This linearity seemingly extends down to the scale of Galactic massive cores in the Milky Way and holds over a total range of luminosity of about eight orders of magnitude (Wu et al. 2005). These results imply that the dense molecular gas (i.e., $n({\rm H_2}) \gtrsim 7 \times 10^4$ cm^{-3}) as traced by the HCN $J = 1 \rightarrow 0$ line, rather than the total molecular gas, is the direct fuel for star formation. High-resolution simulation of dense clouds found that the HCN luminosity is related to mass of dense gas of $\gtrsim 10^4$ cm^{-3} (Onus et al. 2018). In addition, *Spitzer* studies of Galactic molecular clouds also show evidence that star formation is restricted to the dense cores of GMCs (e.g., Evans 2008; Lada et al. 2010). The critical density $n_{\rm crit}$[1] of rotational transitions is proportional to $\mu^2 \nu^3$ (for optically thin lines at frequency ν; μ is the dipole moment of the molecule); therefore molecules with high dipole moment are expected to trace high-density molecular gas (e.g., $\mu_{\rm HCN} \sim 2.98$ D, $\mu_{\rm HCO^+} \sim 3.93$ D, and $\mu_{\rm CS} \sim 1.96$ D versus $\mu_{\rm CO} \sim 0.11$ D; see Schöier et al. 2005). Subsequently, a number of studies have explored the link between molecular lines of dense gas (e.g., HCN, HCO$^+$, and CS) and IR luminosities in different population of galaxies (e.g., Gao et al. 2007; Papadopoulos 2007; Baan et al. 2008; Liu & Gao 2010; Wu et al. 2010; Wang et al. 2011; García-Burillo et al. 2012; Zhang et al. 2014; Chen et al. 2015; Usero et al. 2015; Liu et al. 2016).

While all of these studies generally agree that there is a close link between the dense gas and star formation, the exact nature of the relation is less clear. Specifically, it is not clear whether the star formation efficiency, as gauged by IR/HCN, is indeed universal from GMCs to distant starburst galaxies. While log-linear fits over eight decades in luminosity have been claimed as evidence of such a universality, claims to the contrary have also been made. For example, local (U)LIRGs have been observed to have 3-4 times higher IR/HCN(1-0) ratios than normal galaxies (Graciá-Carpio et al.

2008; García-Burillo et al. 2012), which would suggest a slightly super-linear IR-HCN relation. Furthermore, resolved studies of dense-gas tracers in nearby galaxies have revealed systematic change in IR/HCN(1-0) with galactocentric radius (e.g., Chen et al. 2015; Bigiel et al. 2016).

The physical processes that can affect the observed $L_{\rm IR} - L'_{\rm dense}$ relation fall into two categories. One category contains the physical mechanisms that might compromise the ability of a given molecular transition(e.g., HCN $J = 1 \rightarrow 0$) to trace the dense gas in a consistent manner that can be calibrated. For example, significant enhancements in the HCN abundance due to X-ray driven chemistry on large scales, such as might be found in AGN (e.g., Lepp & Dalgarno 1996; Kohno et al. 2001). The HCN abundance is also thought to be enhanced in hot cores and high-temperature chemistry regions driven by shock heating. Furthermore, it is predicted to be sensitive to the gas phase metallicity (e.g., Bayet et al. 2012; Davis et al. 2013; Braine et al. 2017). In the other category we find physical process that would affect the star formation efficiency. Recent observations of Orion A show that the HCN $J = 1 \rightarrow 0$ emission can trace gas with a characteristic H$_2$ density that is about two orders of magnitude below the value commonly adopted (Kauffmann et al. 2017), which argues that HCN may also can be excited through collisions with electrons(Goldsmith & Kauffmann 2017). It has been argued that the HCN $J = 1 \rightarrow 0$ line could be enhanced by infrared pumping through a vibrational transition at 14 μm near strong mid-infrared sources (e.g., Aalto et al. 1995, 2012; Graciá-Carpio et al. 2006). In addition, self-absorption of HCN emission has been observed in the Galactic Center and in the compact obscured nuclei of nearby (U)LIRGs (Mills et al. 2013; Mills & Battersby 2017; Aalto et al. 2015), thereby rendering this line useless as a probe of the star-forming conditions in the center.

It is still not fully understood how the physical properties of molecular clouds affect the star-formation process in galaxies. In a theoretical study of the star-formation relation, Krumholz & McKee (2005) and Krumholz & Thompson (2007) derive a turbulence-regulated model for understanding the K-S law. They propose that the star formation is controlled by the free-fall timescale of the gas, and that the slope of the IR–molecular line luminosity correlations, i.e., the relation between the SFR as probed by the IR luminosity and the molecular emission line, depends on the average gas density of the molecular clouds and the critical density of the molecular line. Similarly, non-local thermodynamic equilibrium radiative transfer calculations

---

[1] The critical density of rotational level j is defined as $n_{\rm crit}(j) = \frac{\sum_{j>j'} A_{j \rightarrow j'}}{\sum_{j \neq j'} C_{j \rightarrow j'}(T_{\rm kin})}$, where $A_{j \rightarrow j'}$ is the Einstein coefficient for spontaneous emission, $A_{j \rightarrow j'} \propto \mu^2 \nu^3$ in units of s^{-1}, $C_{j \rightarrow j'}$ is the collision rate coefficient that depends on the gas temperature and in units of cm^3 s^{-1}. All critical densities in this work are calculated on the assumption of $T_{\rm kin} = 100$ K and optically thin conditions. The critical densities will decrease if the lines are optically thick.

with hydrodynamical simulations of galaxies predict decreasing power-law indices of the SFR–molecular line luminosity relation with increasing $n_{\rm crit}$, due to the increase of subthermal emission of the gas tracers in galaxies (Narayanan et al. 2008).

Lada et al. (2010, 2012) argue that the rate of star formation in a molecular cloud or galaxy does not depend on the overall average gas density, but only on the amount of molecular gas above a certain volume density or column density thresholds (i.e., $n({\rm H_2}) \geqslant 10^4$ cm^{-3}; see also Heiderman et al. 2010). Observations of local molecular clouds by Evans et al. (2014) show evidence to support this density threshold model and find that the free-fall time ($t_{\rm ff}$) is irrelevant to the SFR on small scales of a few pc within molecular clouds. Zhang et al. (2014) observed HCN $J = 4 \to 3$, HCO$^+$ $J = 4 \to 3$, and CS $J = 7 \to 6$ in 20 nearby star-forming galaxies and found tight linear correlations of IR–molecular line luminosities for all three gas tracers that probe molecular gas with density higher than 10^6 cm^{-3}, consistent with those found for HCN $J = 1 \to 0$ (e.g., Gao & Solomon 2004a,b; Wu et al. 2005) and CS $J = 5 \to 4$ (e.g., Wang et al. 2011) observations, indicating that the free-fall time scale is likely irrelevant to the SFR on global scales for gas with densities $\gtrsim 10^4$ cm^{-3}. They argue that the shorter $t_{\rm ff}$ for the denser gas would not keep $L'_{\rm dense} - L_{\rm IR}$ linear if the $\Sigma_{\rm dense}/t_{\rm ff} - \Sigma_{\rm SFR}$ correlations are linear for all of the dense gas, since the gas content as traced by molecule at high-J (e.g., HCN $J = 4 \to 3$) has a shorter $t_{\rm ff}$ than that at low-J (e.g., HCN $J = 1 \to 0$) with a lower critical density because $t_{\rm ff} \propto \rho^{-1/2}$. However, it is important to remember that the correlation of $\Sigma_{\rm dense} - \Sigma_{\rm SFR}$ is subject to uncertainties in the conversion from $L'_{\rm dense}$ to the gas mass and from $L_{\rm IR}$ to the SFR. In addition, the *Herschel* study of a large sample of nearby galaxies and Galactic clouds in mid-to-high-J ($J = 4 \to 3$ to $12 \to 11$) CO transitions by Liu et al. (2015a) found that all nine CO transitions are linearly correlated with IR luminosities over a luminosity range of about 14 orders of magnitude, from high-z star-forming galaxies down to Galactic young stellar objects. Recent observations of Galactic clouds also found that the dense-gas SFE is remarkably constant over a wide range of scales (i.e., from $\sim 1 - 10$ pc to >10 kpc) and far-ultraviolet radiation environments (Shimajiri et al. 2017).

Up to now, observations of dense gas in galaxies have been mainly performed on the central nuclear regions of nearby galaxies with a single pointing or in local (U)LIRGs with global measures. Observations of dense-gas tracers toward the outer disks of galaxies that are more quiescent and relatively weaker in gas emission

are still scarce. Chen et al. (2015) presented a HCN $J = 1 \to 0$ map of M51 that covers a $4' \times 5'$ region. They found that the outer disk regions of M51 on a kpc-scale follow the IR-HCN relation established globally in galaxies within the scatter and these regions bridge the luminosity gap between GMCs and galaxies. Maps of M51 in HCN, HCO$^+$, and HNC $J = 1 \to 0$ emission were also shown in Bigiel et al. (2016). Both studies show that HCN $J = 1 \to 0$ is enhanced with respect to the IR emission in the nuclear region of M51 compared to the outer disk. These are consistent with the results reported by Kohno et al. (1996), who found the HCN emission is enhanced compared to the CO emission in the central region (<200 pc). It has been suggested that the enhancement of the HCN abundance at the nucleus of M51 could be attributed to the shock produced by the interaction between AGN jets and molecular gas (Matsushita et al. 2015). HCN $J = 1 \to 0$ observations in several off-nuclear positions of nearby galaxies by Usero et al. (2015) show a systematic variation of the SFR per unit dense-gas mass with both the H$_2$ and stellar mass surface densities, which they argue is more consistent with models of turbulence-regulated star formation than with density threshold models.

In this work we present new mapping observations of six nearby star-forming galaxies, NGC 253, NGC 1068, IC 342, M82, M83, NGC 6946, in the $J = 4 \to 3$ lines of HCN and HCO$^+$. These observations were completed in the early stages of the MALATANG (Mapping the dense molecular gas in the strongest star-forming galaxies; Zhang et al. 2018, in prep.) survey with the James Clerk Maxwell Telescope (JCMT). In the MALATANG survey, we select these six targets to be mapped in the central regions because of their broad distribution, strong emission lines of molecular gas, and concentrated star-formation activity in the nuclear regions. Table 1 outlines some of the basic physical properties of these six galaxies. These are the first HCN $J = 4 \to 3$ and HCO$^+$ $J = 4 \to 3$ spatially resolved observations toward the central $2' \times 2'$ region (i.e., $\sim 2 - 9$ kpc) of these nearby galaxies to date. Three of our sample galaxies, i.e., NGC 253, NGC 1068, and M82, have previously been mapped in the $J = 4 \to 3$ lines of HCN and the HCO$^+$ (e.g., Seaquist & Frayer 2000; Knudsen et al. 2007; García-Burillo et al. 2014; Krips et al. 2011) but over on smaller regions. All six galaxies have been mapped in CO $J = 1 \to 0$ by the 45 m telescope of the Nobeyama Radio Observatory (NRO) with almost the same angular resolution as the JCMT (e.g., Nakai et al. 1987; Sorai et al. 2000; Kuno et al. 2007; Salak et al. 2013), providing an excellent comparison with the total H$_2$ gas.

Table 1. The basic properties of the galaxies in the MALATANG sample observed in jiggle-map mode

Source	R.A.(J2000)	Decl.(J2000)	V_{hel}[a]	D[b]	D_{25}[c]	P.A.[d]	Inclination	Spatial Scale	Type[e]	Reference[f]
			(km s^{-1})	(Mpc)	(arcmin)	(deg)	(deg)	(1″)		
NGC 253	00 47 33.1	−25 17 19.7	243	3.5	27.5 × 6.8	51	76	17 pc	SAB(s)c, SF	1
NGC 1068	02 42 40.8	−00 00 47.8	1137	15.7	7.1 × 6.0	90	43	76 pc	(R)SA(rs)b, AGN	⋯
IC 342	03 46 48.5	+68 05 46.0	31	3.4	21.4 × 20.9	0	25	16 pc	SAB(rs)cd, SF	2
M82	09 55 52.4	+69 40 46.9	203	3.5	11.2 × 4.3	65	66	17 pc	I0 sp, SF	3
M83	13 37 00.9	−29 51 56.0	513	4.8	12.9 × 11.5	45	27	23 pc	SAB(s)c, SF	1
NGC 6946	20 34 52.3	+60 09 13.2	40	4.7	11.5 × 9.8	19	30	23 pc	SAB(rs)cd, SF	4,5

[a] Heliocentric velocity drawn from NASA/IPAC Extragalactic Database (NED).

[b] Source distance. For NGC 1068, the distance is calculated using $H_0 = 71$ km s^{-1} Mpc^{-1} corrected for the Virgo infall motion. The distances of the remaining galaxies are recent values from the literature. See the last column for the reference.

[c] Major and minor diameters of the galaxies, which is an optical size measured at the 25$^{\mathrm{th}}$-magnitude isophote in the blue band.

[d] Position angle of the major axis of the galaxy, except for NGC 1068 and IC 342. This is used in mapping HCN and HCO$^+$ emission.

[e] Galaxy types from NED. SF denotes galaxies that are star-forming without an AGN. NGC 1068 is a barred spiral galaxy hosting a Seyfert 2 type AGN.

[f] Reference for the source distance. (1) Radburn-Smith et al. (2011); (2) Wu et al. (2014); (3) Dalcanton et al. (2009); (4) Poznanski et al. (2009); and (5) Olivares E. et al. (2010).

We describe our JCMT observations and the data reduction, and the processing of ancillary data in Section 2. Section 3 presents the spectra and luminosity measurements. In Section 4 the relationships between the dense-molecular-gas tracers and the star-formation properties are presented and discussed. In Section 5, we present the HCN to HCO$^+$ $J = 4 \to 3$ line ratio, and discuss possible explanations for the variations of line ratios in different populations of galaxies. Our main results are summarized in Section 6. We adopt cosmological parameters of $H_0 = 71$ km s^{-1} Mpc^{-1}, $\Omega_{\mathrm{M}} = 0.27$, $\Omega_{\Lambda} = 0.73$ throughout this work (Spergel et al. 2007).

2. OBSERVATIONS AND DATA REDUCTION

2.1. *JCMT HCN(4–3) and HCO$^+$(4–3) Data*

Zhang et al. (2018, in prep.) describe the basic MALATANG observation and reduction strategy. In brief, observations of the $J = 4 \to 3$ lines of HCN and HCO$^+$ in the six galaxies that we are studying here, NGC 253, NGC 1068, IC 342, M82, M83, and NGC 6946, were obtained on the JCMT telescope with the 16-receptor array receiver Heterodyne Array Receiver Program (HARP; Buckle et al. 2009), between 2015 December and 2016 November in the early stages of the MALATANG survey. The Auto-Correlation Spectral Imaging System (ACSIS) spectrometer was used as the receiver backend with a bandwidth of 1 GHz and a

resolution of 0.488 MHz, which correspond to 840 km s^{-1} and 0.41 km s^{-1} at 354 GHz, respectively. We mapped the central $2' \times 2'$ region for all six targets using a 3×3 jiggle mode with grid spacing of 10″. The full width at half maximum (FWHM) beamwidth of each receptor at 350 GHz is about 14″. To optimise the performance, we set up the rotator angle of the K-mirror to control the orientation of the HARP array so that there were four working receptors parallel to the major axis of the galaxy in each scan, since two receptors (H13, H14) at the edge of the array were not operational. The telescope pointing was checked before starting a new source, and every 1-1.5 hours by observing one or more calibrator sources in the CO $J = 3 \to 2$ line at 345.8 GHz. The uncertainty in the absolute flux calibration is estimated to be about 10% for our sample of galaxies and is measured with the standard line calibrators. The velocity of each galaxy measured in our observations is radio defined with respect to the kinematical Local Standard of Rest (LSR). Details of the observations for the six galaxies are summarized in Table 2.

We reduce the data using the Starlink software package ORAC-DR (Jenness et al. 2015) to obtain pipeline-processed data and then convert the spectra

Table 2. A summary of observing parameters

Source	Molecule	Dates of observations	$f_{\rm obs}$	ROT_PA	$\overline{T_{\rm sys}}$	$\overline{\tau}$	$t_{\rm int}$
			(GHz)	(deg)	(K)	(225 GHz)	(min)
(1)	(2)	(3)	(4)	(5)	(6)	(7)	(8)
NGC 253	HCN $J = 4 \to 3$	2015-(12-02,12-10,12-11)	354.223	51, −39	231	0.024	142
	HCO$^+$ $J = 4 \to 3$	2015-12-12	356.447	51, −39	281	0.036	100
NGC 1068	HCN $J = 4 \to 3$	2015-(12-13,12-30,12-31),2016-11-14	353.191	0	246	0.046	250
	HCO$^+$ $J = 4 \to 3$	2015-(12-12,12-13),2016-(02-10,06-23,10-09)	355.411	0	328	0.072	287
IC 342	HCN $J = 4 \to 3$	2015-(12-02,12-12,12-16),2016-(10-08,10-09)	354.474	90	458	0.076	300
	HCO$^+$ $J = 4 \to 3$	2015-(12-13,12-16,12-20,12-21,12-24),2016-10-07	356.701	90	453	0.070	352
M82	HCN $J = 4 \to 3$	2015-(12-10,12-12)	354.265	65, 155	270	0.031	150
	HCO$^+$ $J = 4 \to 3$	2015-12-13	356.494	65, 155	338	0.051	100
M83	HCN $J = 4 \to 3$	2016-(06-22,06-25,07-12,07-13,07-14)	353.954	−45	459	0.075	300
	HCO$^+$ $J = 4 \to 3$	2016-(06-26,07-11,07-15,07-16,07-17,07-18,07-31)	356.132	−45	619	0.097	350
NGC 6946	HCN $J = 4 \to 3$	2016-(05-04,06-15,07-11,07-12)	354.458	109	409	0.082	450
	HCO$^+$ $J = 4 \to 3$	2016-(05-05,05-06,06-16,07-12,07-13,07-14,07-15)	356.681	109	472	0.091	553

NOTE—Column 1: galaxy name. Column 2: observed spectral line. Column 3: the data obtained in the early stage of MALATANG survey that were used in this study. The date of the observations is listed in format of YYYY-MM-DD. Column 4: observing frequency. Column 5: position of the K-mirror. In order to make sure there are four working receptors parallel to the major axis of the galaxies in each scan, we set up the rotator angle of the K-mirror to control the orientation of the HARP array (see Sect. 2.1). Column 6: median system temperature over all observations. Column 7: median atmospheric opacity at 225 GHz over the observations that was recorded at the start and end of each scan. Column 8: total integration time including time spent integrating on the source and the reference position.

to GILDAS/CLASS[2] format for further data processing. A recipe of REDUCE_SCIENCE_BROADLINE with default parameters was adopted for the ORAC-DR pipeline. We further assess the qualify of the data by inspecting the flatness of the baseline and the deviation of the rms noise level between the measured and expected values based on the radiometer equation and then attribute a quality tag to each spectrum. After flagging the data with a bad quality grade (i.e., spectra with distorted baselines or abnormal rms noise levels, which is defined as three times higher than the value calculated with the radiometer equation), the data for each spectral line were gridded into a cube. For positions observed with the central four receptors, on average about 15% of the spectra were flagged due to bad baselines, while about $30 - 40\%$ were discarded for positions observed with receptors on the edge of the array which are less stable. We fitted and subtracted a first-order baseline from the data cube using channels outside of the velocity range of the line emission. The final cubes were converted from antenna temperature $T_{\rm A}^*$ to main beam temperature $T_{\rm mb}$ adopting a main beam efficiency

of $\eta_{\rm mb} = 0.64$ ($T_{\rm mb} \equiv T_{\rm A}^*/\eta_{\rm mb}$). To check the validity of the data processing results with the ORAC-DR pipeline, we used a different reduction method which combines the raw data into a cube using the task `makecube` in SMURF package (Jenness et al. 2013), after first flagging poor data (see Wilson et al. 2012; Warren et al. 2010). Similarly, the spectra were converted to CLASS format for further analysis. Figure 1 is a comparison of the spectra in the central $90'' \times 90''$ region of M82 obtained from the reduction method with the ORAC-DR pipeline with those processed using the method described in Wilson et al. (2012). It is clear that both the profile and the intensity of the spectra derived from different reduction methods are in good agreement for each position where significant signal is detected. A refined data reduction method, which aims primarily at the processing of weak emission lines by converting the raw data to GILDAS/CLASS format and qualifying the data automatically, is under development (Zhang et al. 2018, in prep.).

2.2. Ancillary Data

The six galaxies in this study have a large number of ancillary data available at multiple wavelengths. In this
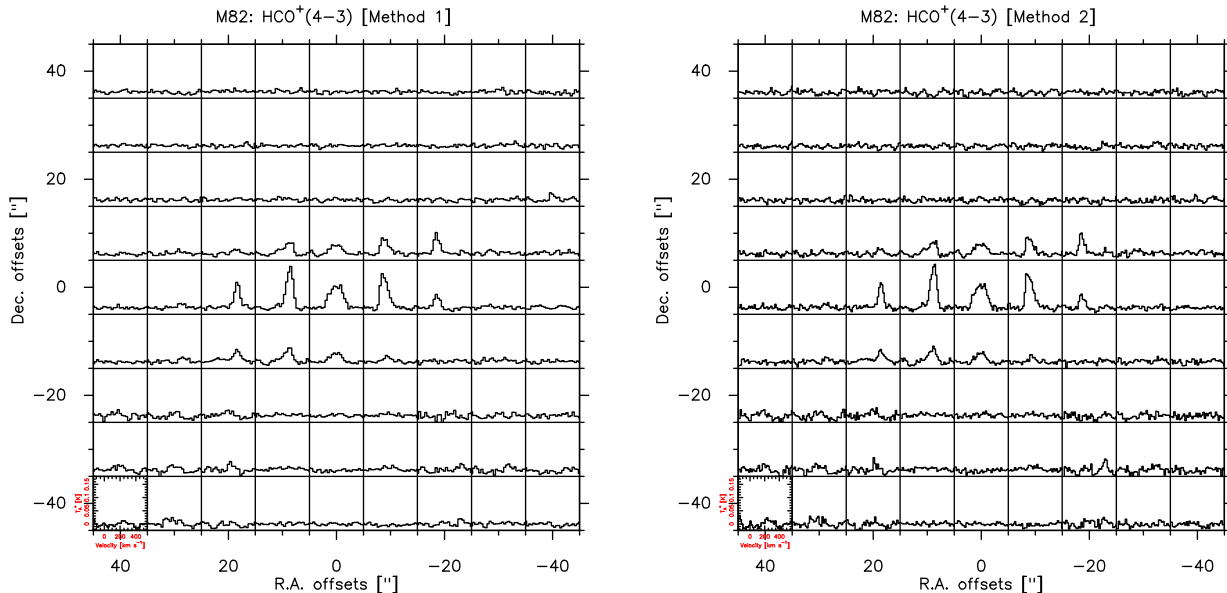
---

[2] http://www.iram.fr/IRAMFR/GILDAS/

Figure 1. JCMT HCO$^+$ $J = 4-3$ spectra map in the central $90'' \times 90''$ region (grid spacing of $10''$) of M82 processed with the ORAC-DR pipeline (left panel) and the method described in Wilson et al. (2012) (right panel). All spectra are on the $T_{\rm A}^*$ scale for the same range from -0.025 K to 0.18 K, and smoothed to 26 km s^{-1} and 20 km s^{-1} for the two methods, respectively.

work, we will focus on molecular line and infrared data for a comprehensive analysis.

2.2.1. *Infrared Data*

We retrieved the calibrated IR image data obtained using the *Spitzer* MIPS and *Herschel* PACS instruments from the NASA/IPAC Infrared Science Archive (IRSA). The data have been processed to level 2 for MIPS 24 μm and level 2.5 for PACS 70 μm, 100 μm, and 160 μm bands in the pipeline. For galaxies that were observed as part of the KINGFISH (Key Insights on Nearby Galaxies: A Far-Infrared Survey with Herschel; Kennicutt et al. (2011)) programme, IC 342 and NGC 6946, we use the PACS images made with the Scanamorphos code version 16.9. The FWHM angular resolutions are approximately $6''.0$, $5''.8$, $7''.8$, and $12''$ at 24 μm, 70 μm, 100 μm, and 160 μm, respectively. The *Herschel* SPIRE data were not used in our study because of their lower angular resolution ($\gtrsim 18''$) compared with our JCMT line observations.

To estimate the infrared luminosity of each position in our target galaxies, we measure the infrared flux densities from 24 μm to 160 μm. In a first step, we use the convolution kernels provided by Aniano et al. (2011) to convolve the *Spitzer* and *Herschel* maps to match the $14''$ beam of our line data. For the PACS data, we scale the image by a factor of $1.133 \times (14/pixel\ size)^2$ where *pixel size* is the length of a pixel in arcseconds, to convert the units from Jy into Jy beam^{-1}, while for MIPS images, we first convert the pixel value in MJy sr^{-1} into Jy and then scale the image to Jy beam^{-1}. We estimate

an average of the pixel values within the sky area to subtract the mean sky background for each galaxy. We then measure the central pixel flux for each position in the convolved image to obtain the flux of each infrared band in units of Jy beam^{-1}.

2.2.2. *NRO 45m CO $J = 1 \rightarrow 0$ Data*

We obtain the CO $J = 1 \rightarrow 0$ data from the Nobeyama CO-mapping survey (Kuno et al. 2007) at the NRO website[3]. The beam size (FWHM=$15''$) of the CO $J = 1 \rightarrow 0$ mapping is comparable to our JCMT observations. We align the CO data with our JCMT data by gridding the cube, and then extract the spectra from each matched position. Except for M82, for which we adopt the CO $J = 3 \rightarrow 2$ data from the JCMT NGLS survey (Wilson et al. 2012), the CO data for the remaining five galaxies are the $J = 1 \rightarrow 0$ transition and were observed with the NRO 45m. With the CO data, we determine for each position the velocity range over which line emission is to be integrated. The CO line is detected at high signal-to-noise ratio, at all positions that we observed with the JCMT. Integrating over the CO emitting velocity ranges guarantees that we have an integrated-intensity measurement along each line of sight, which is particularly important for positions with weak emission of HCN or HCO$^+$ $J = 4 \rightarrow 3$ line.

3. MOLECULAR LINE AND INFRARED MEASUREMENTS

---

[3] http://www.nro.nao.ac.jp/~nro45mrt/html/COatlas/

3.1. *Spectra*

Fig. 2 shows mosaics of HCN $J = 4 \rightarrow 3$ and HCO$^+$ $J = 4 \rightarrow 3$ spectra of the central $\sim 50'' \times 50''$ regions of the six galaxies, which have been mapped in their central $2' \times 2'$ regions. Our observations show that the dense molecular-line emission is mainly concentrated within the central $\sim 1'$ region. We will present a further analysis of the data in the outer disks (i.e., $\gtrsim 1'$ region) using the refined data-reduction method mentioned in Sect. 2.1 in a follow-up paper. All the six galaxies have been detected in both HCN $J = 4 \rightarrow 3$ and HCO$^+$ $J = 4 \rightarrow 3$ lines in off-central positions, except M83 where only the central position was detected in HCN and HCO$^+$ emission with significance of 4.9 σ and 8.5 σ respectively. For M83, we only show the spectral line toward the central position and a spectrum averaged by stacking all the positions observed, excluding the center for each line. For spectrum from each position, we shift the velocity relative to the line center, which is derived from CO $J = 1 \rightarrow 0$ spectra at the same position with a Gaussian fitting, then stack the HCN and HCO$^+$ spectra from all off-center positions. As expected, the line profiles are very similar between HCN and HCO$^+$ since both trace the dense molecular gas in galaxies. For the five galaxies with detections in off-central positions, the rotation of circumnuclear gas is apparent in both lines based on the line profiles and the shifts in centroid velocity.

3.2. *HCN and HCO$^+$ Line Luminosities*

The observed line intensities, $I \equiv \int T_{\mathrm{mb}} dv$, for the positions with $\geqslant 3\,\sigma$ detection in the $J = 4 \rightarrow 3$ lines of HCN and HCO$^+$ are listed in Table 3, along with the line luminosities. We define a detection if the velocity-integrated line intensity is higher than or equal to $3\,\sigma$. The uncertainties (σ) in the integrated intensities were derived via

$$\sigma_I = T_{\mathrm{rms}} \sqrt{\Delta v_{\mathrm{line}} \Delta v_{\mathrm{res}}} \sqrt{1 + \Delta v_{\mathrm{line}}/\Delta v_{\mathrm{base}}}, \quad (1)$$

where T_{rms} is the rms main-beam temperature of the line data for a spectral velocity resolution of Δv_{res}, Δv_{line} is the velocity range of the emission line, and Δv_{base} is the velocity range used to fit the baseline (Gao 1996). The velocity range is determined based on the CO $J = 1 \rightarrow 0$ data with a Gaussian fit to the line profile, on the assumption that the velocity range of dense gas is covered by the CO line emitting range (see Sect. 2.2.2). For the positions without significant detections, we estimated a $3\,\sigma$ upper limit to the line integrated intensities. The CO $J = 1 \rightarrow 0$ luminosities of M82 were estimated based on the JCMT CO $J = 3 \rightarrow 2$ data by assuming a line brightness temperature ratio of $r_{31} = 0.8 \pm 0.2$ for

all the positions mapped in M82 (e.g., Weiß et al. 2005; Mao et al. 2010).

The line luminosities L'_{dense}[4] for each position were calculated following Solomon et al. (1997):

$$\begin{aligned} L'_{\mathrm{dense}} =& 3.25 \times 10^7 \left(\frac{S\Delta v}{1\ \mathrm{Jy\ km\ s^{-1}}} \right) \left(\frac{\nu_{\mathrm{obs}}}{1\ \mathrm{GHz}} \right)^{-2} \\ & \times \left(\frac{D_{\mathrm{L}}}{1\ \mathrm{Mpc}} \right)^2 (1+z)^{-3}\ \mathrm{K\ km\ s^{-1}\ pc^2,} \end{aligned} \quad (2)$$

where $S\Delta v$ is the velocity-integrated flux density, ν_{obs} is the observed line frequency, and D_{L} is the luminosity distance. We convert the line intensity to flux density using a conversion factor of $S/T_{\mathrm{mb}} = 15.6/\eta_{\mathrm{mb}} = 24.4$ Jy K^{-1} for the JCMT telescope by assuming that the line emission from each individual region fills the main beam, given that the gas emission is rather clumpy in these nearby galaxies.

Three of our sample galaxies have published fluxes of HCN and HCO$^+$ $J = 4 \rightarrow 3$ emission towards the galaxy center in the literature (NGC 253, NGC 1068, M82; Zhang et al. 2014; Knudsen et al. 2007; Seaquist & Frayer 2000). We compared our fluxes with those previous efforts and found good agreement for these sources (i.e., agree to within $\sim 20\%$).

3.3. *Infrared Luminosities*

We estimate the total infrared luminosities L_{TIR} from 3 μm to 1100 μm using the prescription of Galametz et al. (2013) based on a combination of *Spitzer*/MIPS 24 μm and *Herschel*/PACS luminosities:

$$L_{\mathrm{TIR}} = \Sigma\, c_i \nu L_\nu(i)\ L_\odot, \quad (3)$$

where $\nu L_\nu(i)$ is the resolved luminosity in a given band i in units of $L_\odot$ and measured as $4\pi D_{\mathrm{L}}^2 (\nu f_\nu)_i$, and c_i are the calibration coefficients for various combinations of *Spitzer* and *Herschel* bands. For galaxies without a MIPS 24 μm image or which are saturated in the 24 μm image cores, we use PACS bands alone to estimate L_{TIR}. With the exception of NGC 1068 and M82, for which only PACS 70 μm and 160 μm data are available, we have photometry data in at least three bands for the remaining four galaxies. The total uncertainties estimated for L_{TIR} comprise the photometric uncertainty, the flux calibration uncertainty (assumed to be 5%; Balog et al. 2014), and the uncertainty of the TIR calibration from combined luminosities ($\sim$20% for galaxies with data in

---

[4] The line luminosity L'_{dense} is often expressed in units of K km s^{-1} pc^2. The line luminosity L_{dense} measured in $L_\odot$ can be converted from L'_{dense} by multiplying a factor of $8\pi k \nu_{\mathrm{rest}}^3/c^3$ (Solomon et al. 1992).
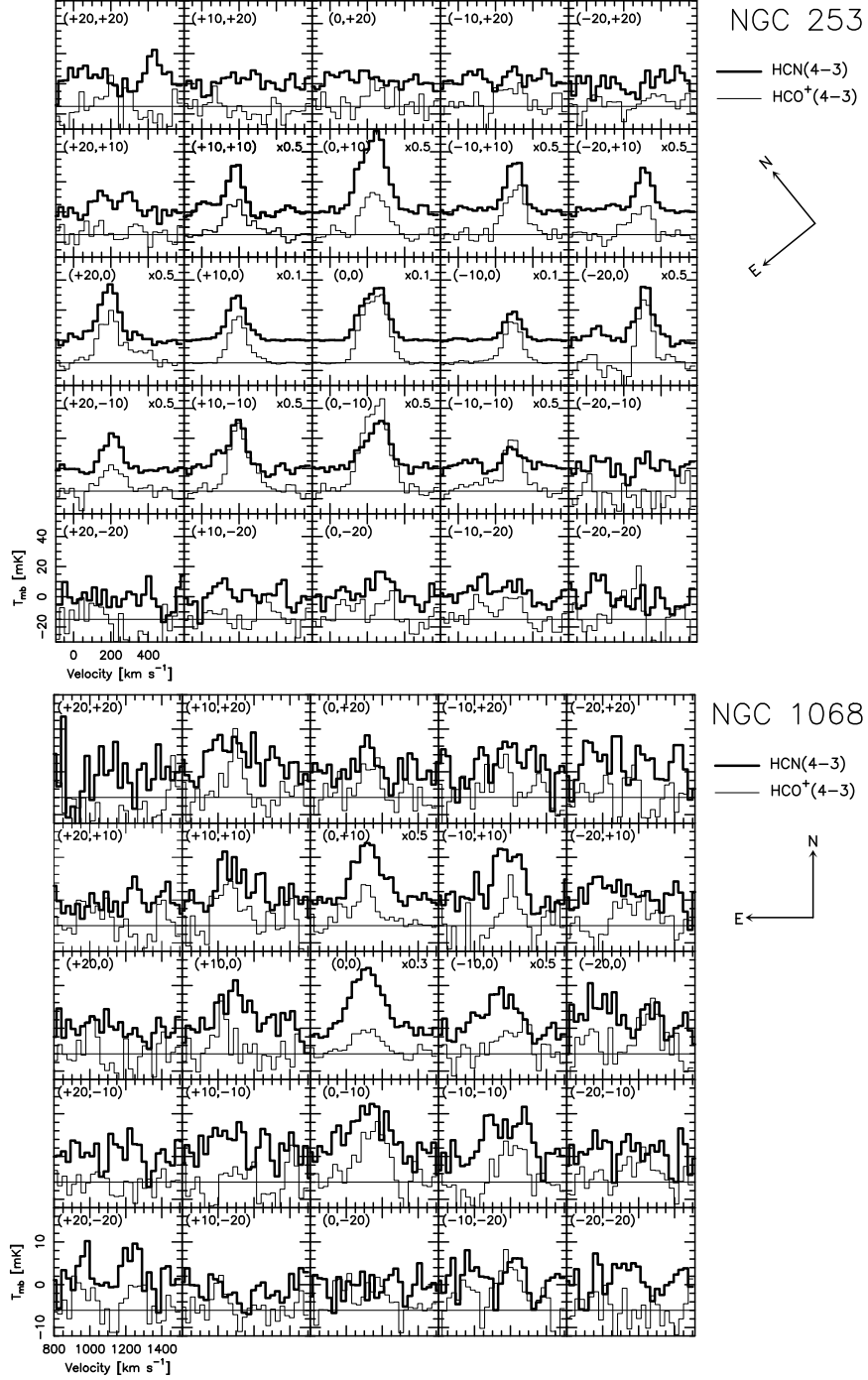
Figure 2. HCN $J = 4 \rightarrow 3$ (*thick lines*) and HCO$^+$ $J = 4 \rightarrow 3$ (*thin lines*) spectra map at the central $\sim 50'' \times 50''$ region of galaxies that were observed in jiggle-mapping mode (3×3 pattern, $10''$ spacing) with the JCMT. To facilitate comparison with the spectra of positions with weak emission, we scaled down the spectra for those positions with relatively stronger emission of both HCN $J = 4 \rightarrow 3$ and HCO$^+$ $J = 4 \rightarrow 3$ by the same multiplying factor which is listed in the upper right of each grid. For each line and position, we averaged all the spectra taken at that position excluding those with poor baseline or abnormal noise levels to produce a final spectrum. All spectra are on the T_{mb} scale and smoothed to a velocity resolution of ~ 26 km s^{-1} unless otherwise noted. The offset from the center position in units of arcsecond is indicated in the upper left of each grid. The HCO$^+$ $J = 4 \rightarrow 3$ lines were shifted downwards with zero intensity level indicated by the horizontal lines. The directions North and East are shown to the right of each spectra grid.
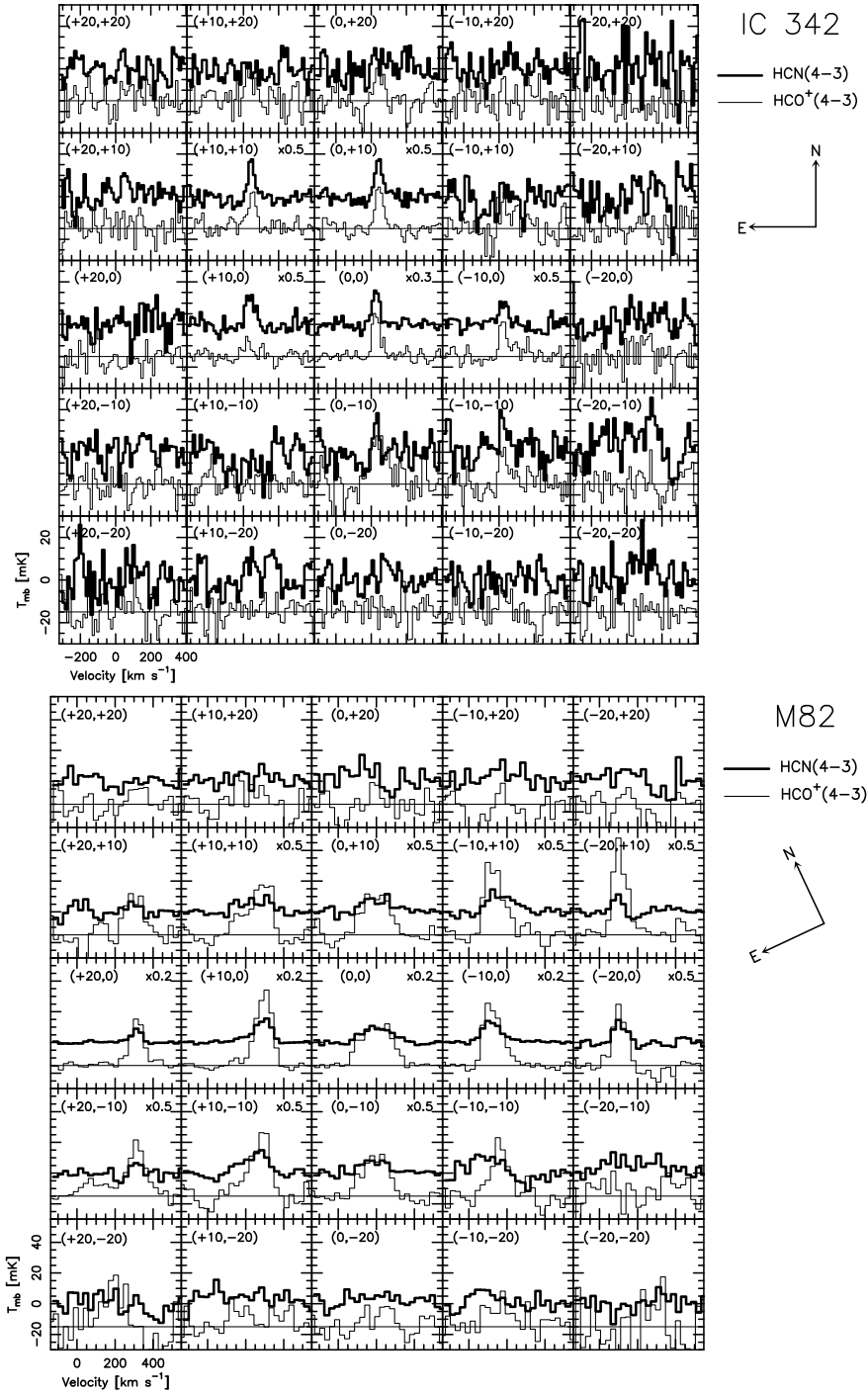
Figure 2. *Continued.* The spectra of IC 342 were smoothed to a velocity resolution of 13 km s^{-1}.
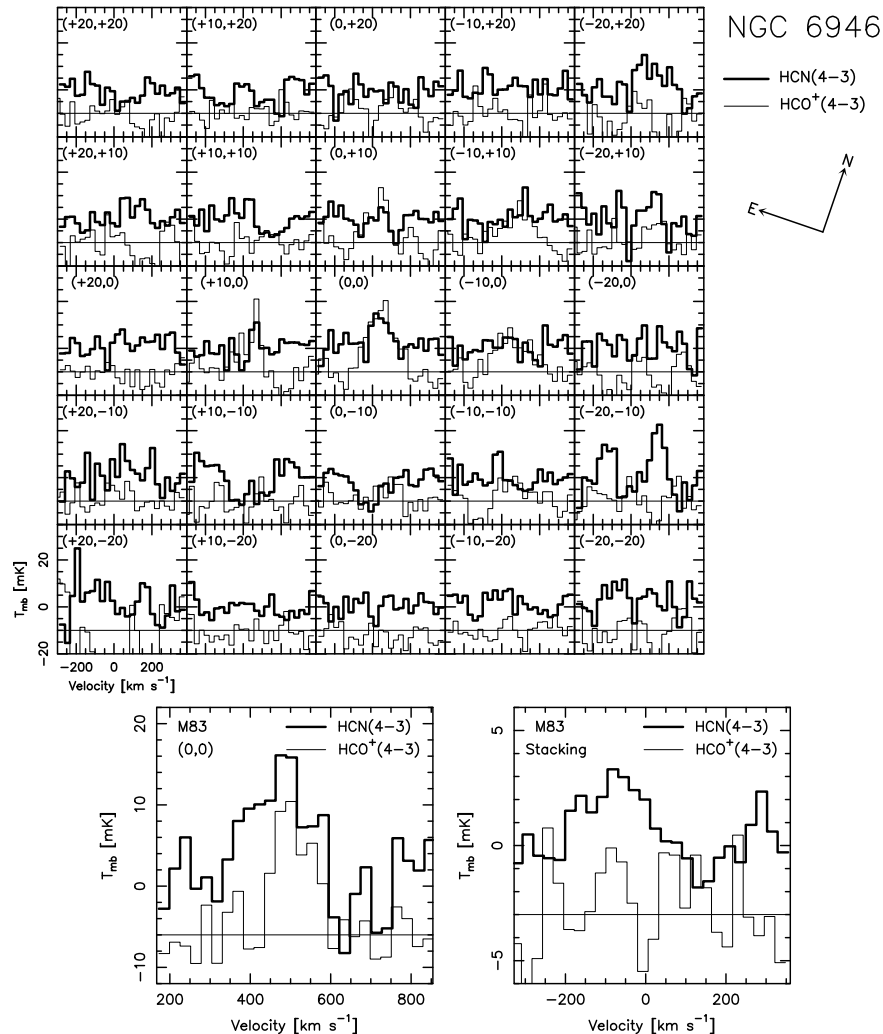
Figure 2. *Continued.* For M83, we show the spectra toward the central position (*left*) and the spectra stacked for all the observed positions excluding the center (*right*). We stack the spectra by averaging the off-center positions with velocities shifted to the line center of the CO $J = 1 \rightarrow 0$ data, which was derived by a single-velocity-component Gaussian fitting.

four IR bands available and $\sim 25\%$ for those have fewer IR images; Galametz et al. 2013). The IR luminosity derived for each position with significant ($\geqslant 3\,\sigma$) HCN $J = 4 \rightarrow 3$ or HCO$^+$ $J = 4 \rightarrow 3$ detections is listed in Table 3.

4. THE RELATIONSHIPS BETWEEN DENSE MOLECULAR GAS TRACERS AND DUST/STAR FORMATION PROPERTIES

4.1. *Correlation Between Molecular Lines of Dense Gas and Infrared Luminosities*

In Fig. 3, we show the $L_{\mathrm{IR}} - L'_{\mathrm{dense}}$ relation for the different populations of galaxies compiled for this work using our new data (Table 3) and the data from the literature, including HCN $J = 4 \rightarrow 3$ and HCO$^+$ $J = 4 \rightarrow 3$ detections in the center of nearby normal galaxies and in (U)LIRGs (Zhang et al. 2014), and six local (U)LIRGs observed with ALMA (Imanishi & Nakanishi 2013a,b, 2014). We also included two high-redshift quasars, the Cloverleaf at $z = 2.56$ and APM 08279+5255 at $z = 3.91$. The Cloverleaf quasar is the only high-z galaxy that is detected in both HCN $J = 4 \rightarrow 3$ and HCO$^+$ $J = 4 \rightarrow 3$ emission (Riechers et al. 2011; Barvainis et al. 1997)[5].

---

[5] Updated measurements of HCN $J = 4 \rightarrow 3$ and HCO$^+$ $J = 4 \rightarrow 3$ emission with the IRAM PdBI for the Cloverleaf were reported by Michel Guélin (2010), and published in the IRAM Newsletter at http://www.iram-institute.org/medias/uploads/NewsletterAug2010.pdf

Tan et al.

Table 3. Derived properties for sampled positions of the six galaxies in our sample

Source	Offsets[a]	$I_{\mathrm{HCN(4-3)}}$	$I_{\mathrm{HCO^+(4-3)}}$	$L'_{\mathrm{HCN(4-3)}}$	$L'_{\mathrm{HCO^+(4-3)}}$	L_{TIR}
	(arcsec)	(K km s^{-1})	(K km s^{-1})	(10^4 K km s^{-1} pc^2)	(10^4 K km s^{-1} pc^2)	(10^7 $L_\odot$)
NGC 253	(0, 0)	57.7 ± 0.7	76.6 ± 0.8	445 ± 5	583 ± 6	1681 ± 102
	(10, 0)	35.9 ± 0.7	36.7 ± 0.5	277 ± 6	280 ± 4	870 ± 53
	(20, 0)	9.8 ± 0.6	9.9 ± 0.9	75 ± 4	76 ± 7	160 ± 9
	(−10, 0)	20.9 ± 0.7	33.0 ± 0.9	162 ± 5	251 ± 7	566 ± 35
	(−20, 0)	7.7 ± 0.7	6.5 ± 0.9	59 ± 6	50 ± 7	64 ± 4
	(0, 10)	17.2 ± 0.6	8.3 ± 0.8	133 ± 5	64 ± 6	1162 ± 71
	(10, 10)	6.3 ± 1.0	6.6 ± 1.0	48 ± 8	50 ± 7	552 ± 33
	(20, 10)	2.2 ± 0.4	< 1.9	17 ± 3	< 14	103 ± 6
	(−10, 10)	8.0 ± 0.4	8.7 ± 0.6	61 ± 3	66 ± 5	509 ± 30
	(−20, 10)	6.4 ± 0.5	4.9 ± 0.6	49 ± 4	37 ± 5	69 ± 4
	(0, −10)	9.9 ± 0.5	20.3 ± 0.8	76 ± 4	154 ± 6	178 ± 11
	(10, −10)	7.6 ± 0.7	11.9 ± 1.0	59 ± 5	91 ± 8	103 ± 6
	(20, −10)	4.4 ± 0.4	3.9 ± 1.0	34 ± 3	30 ± 7	41 ± 2
	(−10, −10)	3.2 ± 0.7	8.6 ± 0.8	25 ± 5	66 ± 6	67 ± 4
NGC 1068	(0, 0)	9.0 ± 0.5	3.4 ± 0.8	1398 ± 72	521 ± 121	4347 ± 280
	(10, 0)	1.6 ± 0.4	< 1.1	245 ± 62	< 165	1511 ± 96
	(−10, 0)	3.8 ± 0.7	2.3 ± 0.6	589 ± 106	346 ± 91	2832 ± 179
	(−20, 0)	< 1.0	1.4 ± 0.4	< 157	208 ± 54	1052 ± 65
	(0, 10)	4.7 ± 0.3	3.2 ± 0.5	721 ± 41	487 ± 71	2675 ± 169
	(10, 10)	1.4 ± 0.3	1.4 ± 0.5	220 ± 53	219 ± 74	1678 ± 105
	(−10, 10)	2.0 ± 0.3	< 1.8	310 ± 41	< 280	1614 ± 101
	(−20, 10)	< 1.0	1.1 ± 0.4	< 150	164 ± 55	627 ± 38
	(0, −10)	2.8 ± 0.5	2.3 ± 0.3	435 ± 74	358 ± 50	1545 ± 96
	(−10, −10)	2.1 ± 0.3	1.4 ± 0.3	329 ± 48	213 ± 53	2018 ± 125
	(−20, −10)	< 0.9	0.9 ± 0.2	< 141	133 ± 33	903 ± 55
	(0, 20)	< 0.9	0.9 ± 0.3	< 139	144 ± 47	1066 ± 66
	(10, 20)	1.7 ± 0.3	1.2 ± 0.4	266 ± 49	188 ± 55	874 ± 54
	(0, −20)	< 1.2	1.6 ± 0.3	< 187	243 ± 50	320 ± 20
	(−10, −20)	< 1.3	1.9 ± 0.6	< 197	284 ± 95	467 ± 30
IC 342	(0, 0)	2.7 ± 0.3	3.8 ± 0.3	20 ± 2	27 ± 2	190 ± 11
	(10, 0)	1.7 ± 0.3	0.8 ± 0.2	12 ± 2	6 ± 2	85 ± 5
	(−10, 0)	1.2 ± 0.2	1.7 ± 0.3	9 ± 2	12 ± 2	87 ± 5
	(0, 10)	1.8 ± 0.2	2.2 ± 0.2	13 ± 1	16 ± 2	99 ± 6
	(10, 10)	1.5 ± 0.2	1.9 ± 0.2	11 ± 2	14 ± 2	49 ± 3
	(−10, 10)	< 0.9	0.8 ± 0.2	< 6	6 ± 2	42 ± 2
	(0, −10)	< 0.7	1.7 ± 0.3	< 5	12 ± 2	55 ± 3
	(−10, −10)	0.9 ± 0.3	0.8 ± 0.2	6 ± 2	6 ± 1	30 ± 2
	(0, 20)	< 0.8	0.9 ± 0.2	< 6	7 ± 2	13 ± 1
	(10, 20)	< 0.7	0.9 ± 0.2	< 5	6 ± 2	11 ± 1

Table 3 continued

Table 3 (continued)

Source	Offsets[a]	$I_{\mathrm{HCN}(4-3)}$	$I_{\mathrm{HCO^+}(4-3)}$	$L'_{\mathrm{HCN}(4-3)}$	$L'_{\mathrm{HCO^+}(4-3)}$	L_{TIR}
	(arcsec)	(K km s^{-1})	(K km s^{-1})	(10^4 K km s^{-1} pc^2)	(10^4 K km s^{-1} pc^2)	($10^7 L_\odot$)
M82	(0, 0)	9.2 ± 0.7	26.3 ± 0.7	71 ± 6	200 ± 5	1052 ± 68
	(10, 0)	8.9 ± 0.4	25.5 ± 0.8	69 ± 3	194 ± 6	785 ± 51
	(20, 0)	3.0 ± 0.4	13.6 ± 0.8	23 ± 3	103 ± 6	323 ± 21
	(−10, 0)	8.3 ± 0.4	23.4 ± 0.9	64 ± 3	179 ± 7	860 ± 57
	(−20, 0)	1.8 ± 0.5	5.8 ± 0.8	14 ± 4	44 ± 6	343 ± 22
	(0, 10)	3.0 ± 0.5	9.0 ± 1.1	23 ± 4	69 ± 9	957 ± 61
	(10, 10)	3.0 ± 0.3	9.9 ± 1.0	23 ± 2	75 ± 8	643 ± 41
	(20, 10)	< 1.5	3.3 ± 0.9	< 11	25 ± 7	295 ± 19
	(−10, 10)	3.7 ± 0.7	11.6 ± 0.9	29 ± 5	88 ± 7	991 ± 63
	(−20, 10)	1.3 ± 0.2	10.6 ± 0.8	10 ± 2	81 ± 6	581 ± 37
	(0, −10)	2.7 ± 0.5	8.6 ± 0.6	21 ± 4	66 ± 5	182 ± 12
	(10, −10)	3.8 ± 0.5	10.8 ± 1.6	29 ± 4	83 ± 12	171 ± 11
	(20, −10)	< 1.6	8.5 ± 0.9	< 12	65 ± 7	86 ± 6
	(−10, −10)	< 1.5	3.8 ± 0.7	< 11	29 ± 5	129 ± 9
	(−20, −10)	1.6 ± 0.4	< 2.4	13 ± 3	< 18	75 ± 5
	(−10, −20)	< 1.7	1.8 ± 0.6	< 13	14 ± 5	31 ± 2
M83	(0, 0)	2.0 ± 0.4	1.7 ± 0.2	29 ± 5	24 ± 3	274 ± 16
NGC 6946	(0, 0)	1.4 ± 0.5	4.5 ± 0.5	20 ± 7	63 ± 7	196 ± 11
	(10, 0)	< 1.0	2.0 ± 0.5	< 14	27 ± 8	44 ± 2
	(−10, 0)	< 1.4	3.1 ± 0.4	< 19	43 ± 6	121 ± 7
	(0, 10)	< 1.2	2.2 ± 0.7	< 16	30 ± 9	77 ± 4
	(−10, 10)	< 1.3	2.4 ± 0.5	< 19	33 ± 7	59 ± 3

Note—All uncertainties are estimated statistically from the measurements. For the line velocity-integrated intensity and luminosity, an additional 10% uncertainty should be added to account for the systematic uncertainties in absolute flux calibration. For the IR luminosity, we need to take into account the additional uncertainties from the flux calibration ($\sim 5\%$) and the TIR calibration ($\sim 20 - 25\%$) (see Sect. 3.3). We report a 3σ upper limit for non-detections.

[a]Offsets without correcting for the rotation of the receiver array. See the observing settings in Sect. 2.1 and the directions North and East for each galaxy in Fig. 2.

For APM 08279+5255, we estimate the HCN $J = 4 \to 3$ and the HCO$^+$ $J = 4 \to 3$ line luminosities based on the $J = 6 \to 5$ lines of HCN and HCO$^+$ measured by Riechers et al. (2010), by assuming a $J = 6 \to 5/J = 4 \to 3$ line luminosity ratio of 1.1±0.6, for both HCN and HCO$^+$. This line ratio is roughly estimated by taking the average of the HCN $J = 6 \to 5/J = 5 \to 4$ luminosity ratio ($r_{65(\mathrm{HCN})} = 1.36 \pm 0.31$; Riechers et al. 2010) and the CO line ratio ($r_{64(\mathrm{CO})} = 0.86 \pm 0.29$; Weiß et al. 2007). Note that it is likely that the uncertainties in the $J = 6 \to 5/J = 4 \to 3$ line ratios are underestimated due to the presumably non-uniform physical conditions in the molecular gas as traced by CO and the dense gas as traced by HCN and HCO$^+$

in this galaxy (Weiß et al. 2007). The SFR are calibrated based on the total IR luminosity (e.g., Kennicutt 1998; Murphy et al. 2011). For the high-z quasars, however, we used the far-IR luminosity (i.e., integrated from 40 μm to 120 μm rest-wavelength, Helou et al. 1985) as a measure of SFR due to the powerful AGN heating of dust in the mid-IR band. The IR luminosity of these two quasars shown in Fig. 3 thus corresponds to the far-IR luminosity plus an additional uncertainty of 30% from converting the FIR luminosity to the total IR luminosity (Weiß et al. 2003, 2007; Sanders et al. 2003). We note that a tentative detection of HCO$^+$ $J = 4 \to 3$ and upper limit of HCN $J = 4 \to 3$ emission in a $z = 2.64$ lensed star-forming galaxy was reported recently by Roberts-Borsani et al. (2017), and stacked detections of
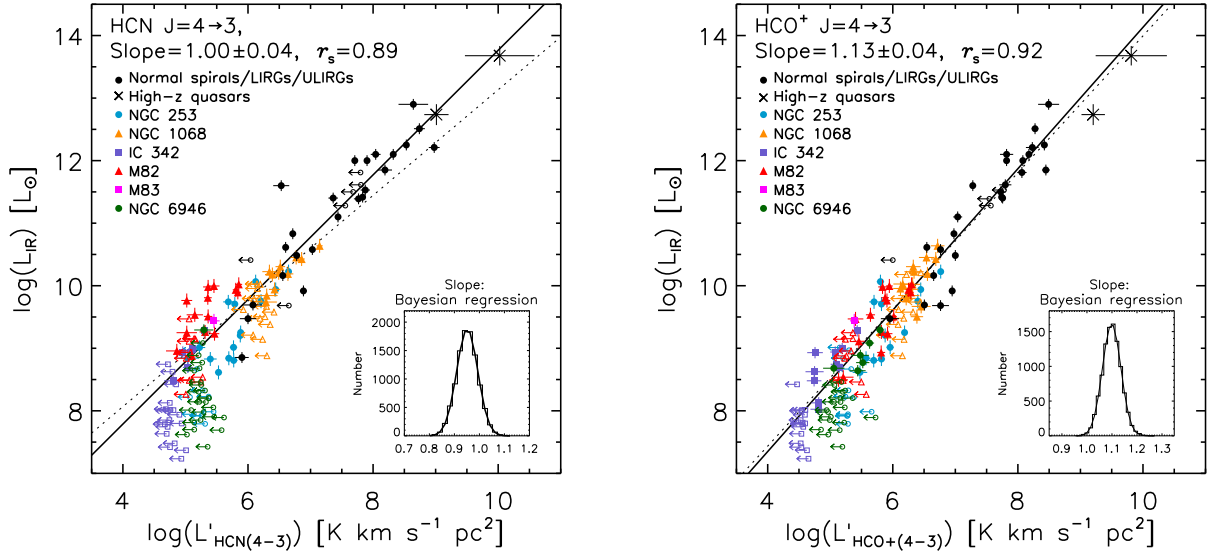
Figure 3. Correlations between the molecular line luminosities of dense-gas tracers $\log(L'_{\rm dense})$ and the IR luminosity $\log(L_{\rm IR})$ for galaxies spatially resolved on sub-kpc scales (*colored symbols*) and galaxies with integrated measurements (*black symbols*). *Left*: HCN $J = 4 \rightarrow 3$. *Right*: HCO$^+$ $J = 4 \rightarrow 3$. The colored symbols represent the spatially resolved sub-kpc structures in the central $\sim 50'' \times 50''$ region of our sample galaxies, and the black symbols indicate the data from the literature (see legend in the top left of each panel). The solid lines in the left and right panels indicate the best-fit relations of Equations (4) and (5) respectively, while the black dotted lines show the relation considering the new JCMT data alone. The upper limits are marked with open symbols with leftward arrows and are not included in the fitting. The total uncertainties on the individual data points, including the statistical measurement uncertainties and the systematic uncertainties, are indicated by error bars (see Table 3). The best-fit power-law index and the Spearman rank correlation coefficient for the $L_{\rm IR} - L'_{\rm HCN(4-3)}$ and the $L_{\rm IR} - L'_{\rm HCO^+(4-3)}$ relation are listed in the top left of each panel. The inset shows the probability density distribution of the slope derived from the Bayesian fitting.

these two lines are reported in high-z dusty galaxies by Spilker et al. (2014). These data were not included in our analysis as no IR measurements are yet available.

We adopt the IDL routine `linfitex.pro` of the MP-FIT package (Markwardt 2009) for the linear least-squares fit and LINMIX_ERR of Kelly (2007) which uses the Markov Chain Monte Carlo approach to account for measurement uncertainties for the Bayesian regression. The uncertainties in $L_{\rm IR}$ and $L'_{\rm dense}$ accounted for in the fitting include the statistical measurement uncertainties and the systematic uncertainties which mainly originate from calibration (see Sect. 2.1 and Sect. 3.3 for details). The best linear least-squares fit (logarithmic) to our new data (the upper limits are not included in the fitting, marked in open symbols with leftward arrows in Fig. 3) combined with the literature data yields

$$\log L_{\rm IR} = 1.00(\pm0.04)\log L'_{\rm HCN(4-3)} + 3.80(\pm0.27). \quad (4)$$

This fit is shown as the solid line in Fig. 3 (left). A Spearman rank correlation test yields a correlation coefficient of $r_{\rm s} = 0.89$, with a probability (p-value) of 1.1×10^{-26} for the null hypothesis. The Bayesian regression fits give a slope of 0.95 ± 0.04, consistent with the linear least-squares fit, and the posterior distribution of possible

slopes is shown in the inset of Fig. 3 (left). A linear least-squares fit to our JCMT data (*colored symbols*) alone yields $\log L_{\rm IR} = 0.84(\pm0.09)\log L'_{\rm HCN(4-3)} + 4.69(\pm0.53)$ and with a Spearman rank correlation coefficient of 0.75, which is shown as a black dotted line in Fig. 3 (left).

In Fig. 3 (right) we plot the relation between $L_{\rm IR}$ and $L'_{\rm HCO^+(4-3)}$ and perform the same comparison. A linear least-squares fit to the data points excluding the upper limits gives a correlation close to linear,

$$\log L_{\rm IR} = 1.13(\pm0.04)\log L'_{\rm HCO^+(4-3)} + 2.83(\pm0.24), \quad (5)$$

with a Spearman rank correlation coefficient of 0.92. The Bayesian regression fits give a similar slope of 1.10 ± 0.04 and the fit using measurements in Table 3 alone gives a consistent relation with $\log L_{\rm IR} = 1.09(\pm0.08)\log L'_{\rm HCO^+(4-3)} + 3.06(\pm0.49)$ and with a Spearman rank correlation coefficient of 0.84.

Liu et al. (2016) observed HCN $J = 4 \rightarrow 3$ and CS $J = 7 \rightarrow 6$ lines in Galactic clumps and found that the $L_{\rm IR}$ are tightly correlated with both HCN and CS luminosities down to clumps with $L_{\rm IR} \sim 10^3 \ L_\odot$. We compiled the HCN $J = 4 \rightarrow 3$ data of Galactic clumps to compare with the data shown in Fig. 3 (left). A linear least-squares fit to all data yields a slope of 1.03 ± 0.01
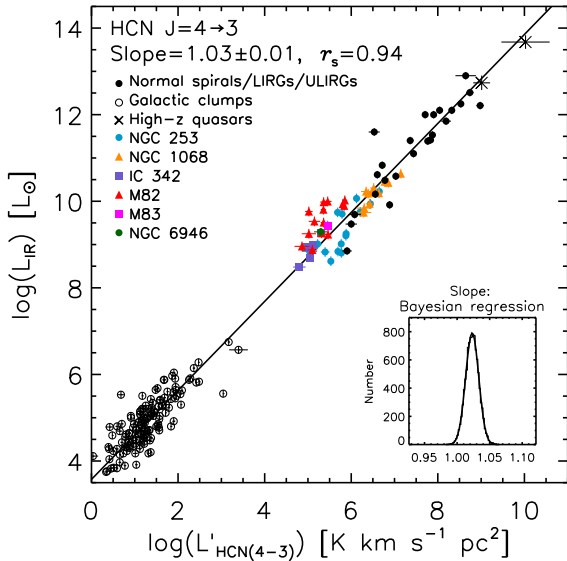
Figure 4. Correlation between HCN $J = 4 \to 3$ and IR luminosities for Galactic clumps (*circles*), our sample of galaxies resolved at sub-kpc scales (*colored symbols*), normal galaxies and local (U)LIRGs (*solid circles*), and high-z quasars (*crosses*). The upper limits of HCN $J = 4 \to 3$ are not included in the fitting and are not shown in this plot. The solid line represents the best-fit relation of $\log L_{\rm IR} = 1.03(\pm0.01)\log L'_{\rm HCN(4-3)} + 3.58$. The probability density distribution of the slope derived from the Bayesian fitting is shown in the inset panel. A Spearman rank correlation analysis yields a correlation coefficient of 0.94.

(see Fig. 4), in good agreement with the fit for the sample of galaxies measured globally.

To check the reliability of the best-fit relations obtained above, we adopted a Monte Carlo (MC) approach to fit the data. This approach, which is based on Blanc et al. (2009) and Leroy et al. (2013), includes observational uncertainties, upper limits, and intrinsic scatter in the fits. Following Blanc et al. (2009) we fitted the following relation with three parameters

$$\left(\frac{L_{\rm IR}}{L_\odot}\right) = A \left(\frac{L'_{\rm gas}}{\rm K\ km\ s^{-1}\ pc^2}\right)^N \times 10^{\mathcal{N}(0,\epsilon)} \quad (6)$$

where A is the normalization factor, N is the power-law index, and $\mathcal{N}(0,\epsilon)$ is the intrinsic, log-normally distributed scatter on the relation with zero mean and standard deviation ϵ. Our data are mainly limited by the sensitivity of the dense-gas observations as can be seen in Fig. 3. For the non-detections of HCN $J = 4 \to 3$ and HCO$^+$ $J = 4 \to 3$ emission, we use the measurements in our fits and exclude data with velocity-integrated intensity $I_{\rm gas} \le 0$. Similarly to Leroy et al. (2013), we grid our data in $\log_{10}(L_{\rm IR}) - \log_{10}(L'_{\rm gas})$ space using cells 0.75 dex wide in both dimensions.

Table 4. Results of Monte Carlo Fitting to Equation(6)

Molecule	$\log_{10} A$	N	ϵ
	$(L_\odot)$		(dex)
HCN $J = 4 \to 3$	3.58±0.25	1.00±0.04	0.53±0.04
HCO$^+$ $J = 4 \to 3$	2.95±0.34	1.10±0.04	0.32±0.11

NOTE—The Best-fit values for parameters in Equation(6) for the $L_{\rm IR} - L'_{\rm HCN(4-3)}$ and the $L_{\rm IR} - L'_{\rm HCO+(4-3)}$ relations. The uncertainties are estimated from a bootstrapping approach described in Appendix A.

The detailed fitting procedure to our data using a MC approach is described in Appendix A. Table 4 reports the results of the MC fits for different dense-gas tracers. For the $L_{\rm IR} - L'_{\rm HCN(4-3)}$ relation we measure a power-law index $N = 1.00\pm0.04$, an amplitude $A = 10^{3.58\pm0.25}$, and an intrinsic scatter $\epsilon = 0.53 \pm 0.04$ dex, while for the $L_{\rm IR} - L'_{\rm HCO+(4-3)}$ relation we obtain a power-law index $N = 1.10 \pm 0.04$, an amplitude $A = 10^{2.95\pm0.34}$, and an intrinsic scatter $\epsilon = 0.32 \pm 0.11$ dex. The best-fit slope and amplitude are in good agreement with the results obtained based on the bivariate linear fit using clipped data in Fig. 3. The intrinsic scatter of 0.53 ± 0.04 dex and 0.32 ± 0.11 dex derived based on the MC fits is significant, implying that the IR luminosity can vary by a factor of $\sim 2-4$ for regions having the same dense molecular line luminosity.

4.2. *Comparison of Correlations Between the Ratios*

To eliminate the distance and the galaxy size dependencies that could introduce a potentially strong correlation of $L_{\rm IR}$ with $L'_{\rm dense}$, where the dense gas is traced by the HCN $J = 4 \to 3$ and the HCO$^+$ $J = 4 \to 3$ emission, we follow the same approach as that adopted by Gao & Solomon (2004b) to examine the correlation between the luminosity ratios $L_{\rm IR}/L'_{\rm CO}$ and $L'_{\rm dense}/L'_{\rm CO}$. A linear least-squares fit to our data including global measurements of local (U)LIRGs and high-z quasars gives slopes of 1.27 ± 0.15 and 1.45 ± 0.15, respectively. A Spearman test yields a correlation coefficient of $r_{\rm s} = 0.57$ with the significance of its deviation from the zero of a p-value of 2.6×10^{-6} for HCN $J = 4 \to 3$, and $r_{\rm s} = 0.65$ with a p-value of 5.3×10^{-10} for HCO$^+$ $J = 4 \to 3$, suggesting a moderately significant correlation between $L_{\rm IR}/L'_{\rm CO}$ and $L'_{\rm dense}/L'_{\rm CO}$ (see Fig. 5 (top)).

Similarly, in Fig. 5 (bottom) we plot the correlation between $L_{\rm IR}$ and $L'_{\rm CO}$ divided by $L'_{\rm dense}$ for normalization. The correlation between $L_{\rm IR}/L'_{\rm HCN(4-3)}$ and $L'_{\rm CO}/L'_{\rm HCN(4-3)}$ is found to be weaker ($r_{\rm s} = 0.36$) than
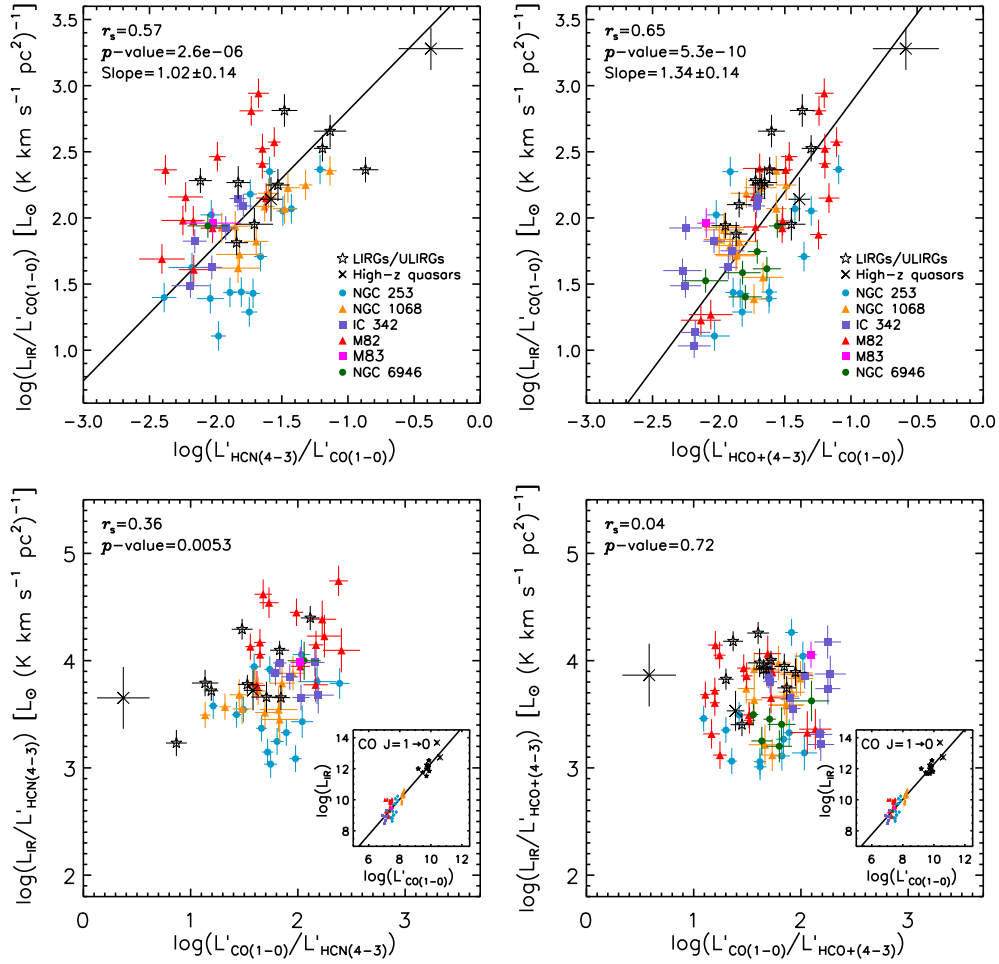
Figure 5. *Top row*: $L_{IR}/L'_{CO(1-0)}$ as a function of $L'_{HCN(4-3)}/L'_{CO(1-0)}$ (*top left*) and $L'_{HCO^+(4-3)}/L'_{CO(1-0)}$ (*top right*) for nearby star-forming galaxies (*colored symbols*), local (U)LIRGs (*open stars*), and high-z quasars (*crosses*). The IR and dense molecular line luminosities are normalized by $L'_{CO(1-0)}$ to remove the galaxy distance and size dependencies. *Bottom row*: similar to the top panels, but instead normalized by HCN $J = 4 \to 3$ (bottom-left panel) and HCO$^+$ $J = 4 \to 3$ (bottom-right panel) instead. The inset shows the correlation between L_{IR} and $L'_{CO(1-0)}$. The Spearman rank correlation coefficient for each panel is listed at the top left.

the correlation between L_{IR} and $L'_{HCN(4-3)}$ normalized by L'_{CO}, and with a higher p-value of 0.0053. For the correlation between $L_{IR}/L'_{HCO^+(4-3)}$ and $L'_{CO}/L'_{HCO^+(4-3)}$, the Spearman test gives a correlation coefficient of 0.04 with a p-value of 0.72, suggesting that the significance of the correlation between the luminosity ratios is very low, although a strong correlation is seen between IR and CO (see the insets in Fig. 5 (bottom)).

The results of this work are limited by the dynamical range of the L'_{dense}/L'_{CO} ratio (about 2 dex) and the large scatter, as well as the effect of correlated axes (both normalized with a same variable), it remains unclear how strong the physical correlation between SFR and dense gas is. It is beyond the scope of this paper to analyze in detail the origin of the possible physical

correlation. Our results are consistent with the correlation between the IR and the HCN(1-0) luminosities shown in Gao & Solomon (2004b). Moreover, a tight linear correlation between the surface densities of the dense molecular gas and the SF rates, as well as between the HCN luminosity and the radio continuum luminosity, has been established for a large sample of galaxies (e.g., Liu & Gao 2010; Liu et al. 2015b; Chen et al. 2015, 2017). All of these results indicate that the star formation is very much likely physically related to the dense molecular gas.

To statistically quantify the detailed physical relationship between dense molecular gas and star formation with models, analysis of the entire dataset of MALATANG and the combination of all datasets from available dense gas surveys (e.g., Gao & Solomon 2004a,b;

Zhang et al. 2014; Usero et al. 2015; Bigiel et al. 2016), and the investigation of the dependence on different parameters are required. We will address this subject in future work.

4.3. Comparison with Literature Data

The nearly unity power-law slopes derived for the $L_{\rm IR} - L'_{\rm HCN(4-3)}$ and the $L_{\rm IR} - L'_{\rm HCO^+(4-3)}$ correlations from our fits are in good agreement with Zhang et al. (2014). The slightly super-linear slope of the $L_{\rm IR} - L'_{\rm HCO^+(4-3)}$ correlation derived from our fit also agrees with that obtained by Zhang et al. (2014), who speculate the super-linear slope is likely to be a result of a decrease of the HCO$^+$ abundance in extreme physical conditions. For example, in extreme IR luminous galaxies, an increase of free electrons created by cosmic-ray ionization would accelerate the destruction of HCO$^+$ by dissociative recombination (Seaquist & Frayer 2000). The self-absorption feature of HCO$^+$ emission line is often observed in the Galactic dense clumps (e.g., Reiter et al. 2011). However, it is not easy to investigate thoroughly the physical origin, since HCO$^+$ is an ion and follows a more complex chemistry (Omont 2007; Papadopoulos 2007). Observations of other molecular ions that probe dense gas, such as N_2H^+, would provide clues to test the hypothesis.

Nevertheless, the linear correlation between $L_{\rm IR}$ and $L'_{\rm HCN(4-3)}$ is similar to that derived for the $J = 1 \to 0$ lines of HCN and HCO$^+$ (e.g., Gao & Solomon 2004b; Wu et al. 2005; Baan et al. 2008; Bigiel et al. 2015, 2016; Usero et al. 2015; Chen et al. 2017) and the CS $J = 7 \to 6$ line (Zhang et al. 2014). All of these correlations hold over a wide IR luminosity range covering nearly 10 orders of magnitude, providing evidence to support the argument that the SFR is directly proportional to the total mass of dense gas, and does not depend on the exact value of the gas density once the gas is denser than a threshold density of $\sim 10^4$ cm^{-3} (Lada et al. 2012). All of these dense-gas tracers have a critical density higher than this threshold and the critical densities ($n_{\rm crit} \sim (3-6) \times 10^6$ cm^{-3}) for HCN $J = 4 \to 3$ and CS $J = 7 \to 6$ are about two orders of magnitude higher than HCN $J = 1 \to 0$. These results are inconsistent with the sub-linear relations (e.g., power-law slope of 0.6±0.1 and 0.7±0.1 for the $L_{\rm IR} - L'_{\rm HCN(4-3)}$ and the $L_{\rm IR} - L'_{\rm HCO^+(4-3)}$ relations, respectively) predicted by numerical simulations, which concluded that the SFR$-L'_{\rm gas}$ slope tends to decrease with increasing $n_{\rm crit}$ (Narayanan et al. 2008; Juneau et al. 2009). Our mapping observations show direct evidence that a portion of dense gas as traced by the HCN $J = 4 \to 3$ and the HCO$^+$ $J = 4 \to 3$ emission

is distributed in the off-nuclear regions. It thus cannot be ruled out that the sub-linear slope ($\sim 0.8 \pm 0.1$) obtained by Bussmann et al. (2008) is a result of underestimating of the total HCN $J = 3 \to 2$ emission for nearby galaxies, as the line intensities are measured from a single point toward the galaxy center with beam size of $\sim 30''$, while the IR luminosities are derived from IRAS flux densities that measured with a larger beam size.

4.4. Variation in the Infrared-to-Molecular-Line Luminosity Ratio

In Fig. 6 (left) we show the ratio of $L_{\rm IR}/L'_{\rm HCN(4-3)}$ as a function of $L_{\rm IR}$. The mean value of $\log(L_{\rm IR}/L'_{\rm HCN(4-3)})$ for Galactic clumps, normal star-forming galaxies, and (U)LIRGs/high-z quasars are 3.62±0.03, 3.89±0.06, and 3.86±0.10, with an rms scatter of 0.35 dex, 0.35 dex, and 0.32 dex, respectively. The mean value of $\log(L_{\rm IR}/L'_{\rm HCN(4-3)})$ for the full sample of galaxies is 3.71±0.03, with an rms scatter of 0.38 dex. The ratio of $L_{\rm IR}/L'_{\rm HCO^+(4-3)}$ shows a similar scatter (see Fig. 6 (right)). The mean $\log(L_{\rm IR}/L'_{\rm HCO^+(4-3)})$ for normal galaxies and (U)LIRGs/high-z quasars are 3.77±0.05 and 4.02±0.08 with an rms scatter of 0.33 dex and 0.26 dex respectively, while the mean value measured for the full sample is 3.73±0.04 with an rms scatter of 0.36 dex. The mean $L_{\rm IR}/L'_{\rm dense}$ ratio measured across the whole population of galaxies in our sample appears to vary little. This is similar to the IR/HCN(1-0) and the IR/HCO$^+$(1-0) data, which are found to be independent of $L_{\rm IR}$ extending from galaxy scales to individual GMCs (e.g., Gao & Solomon 2004b; Wu et al. 2005; Chen et al. 2017). Note that there is significant scatter measured within our sample of galaxies, which is in good agreement with the intrinsic scatter derived from MC fitting (see Sect. 4.1). A plausible explanation for the large scatter could be a wide range of physical conditions for the molecular gas in the dense phase and/or abundance variations (e.g., Jackson et al. 1995; Papadopoulos 2007). However, it is worth noting that both the IR/HCN(4-3) and the IR/HCO$^+$(4-3) ratios show systematic variations with IR luminosity within individual spatially resolved galaxies, and also the Galactic clumps, though with significant scatter. We discuss possible explanations for these trends in the next subsection.

Compared with other galaxies in our sample, M82 appear weakened in HCN(4-3) relative to IR with ratio of IR/HCN(4-3) mostly above 1 σ scatter (see Fig. 6 (left)), while the IR/HCO$^+$(4-3) ratio shown in Fig. 6 (right) is well within the 1 σ scatter. A plausible explanation for the decrease of $L'_{\rm HCN(4-3)}/L'_{\rm HCO^+(4-3)}$ could be a
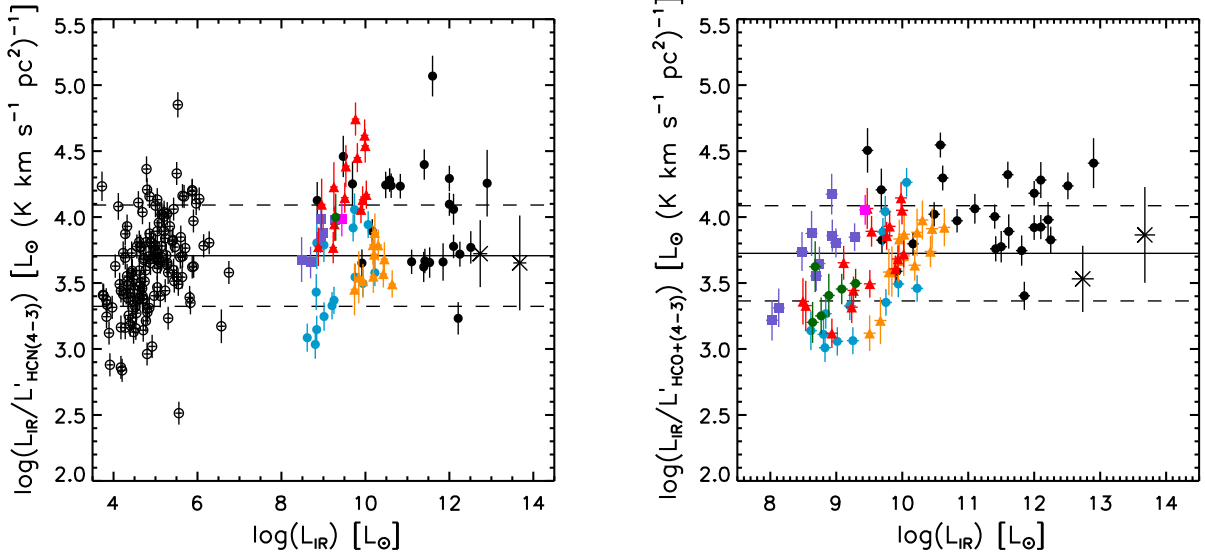
Figure 6. *Left*: the luminosity ratio of IR to HCN(4-3) as a function of L_{IR} for Galactic clumps (*circles*), our sample of galaxies resolved to sub-kpc scales (*colored symbols*), normal galaxies and local (U)LIRGs (*solid circles*), and high-z quasars (*crosses*). *Right*: the luminosity ratio of IR to HCO$^+$(4-3) as a function of L_{IR} for the same set of galaxies as in the left panel, but without the sample of Galactic clumps. Symbols are as in Fig. 4. The mean values of $\log(L_{IR}/L'_{HCN(4-3)})$ and $\log(L_{IR}/L'_{HCO^+(4-3)})$ for the full sample of galaxies are 3.71±0.03 and 3.73±0.04 (*solid lines*), with an rms scatter of 0.38 dex and 0.36 dex (*dashed lines*), respectively.

low HCN abundance in M82. Braine et al. (2017) observed various molecular lines in low-metallicity Local Group galaxies and found that both HCN and HNC lines are weak with respect to the IR emission, while HCO$^+$ follows the trends observed in galaxies with solar metallicity. They attributed the weakness of the nitrogen bearing molecules to the low nitrogen abundance in these galaxies, based on the observed trend in the HCN/HCO$^+$ ratio with metallicity. The weak HCN $J = 4 \rightarrow 3$ emission observed in M82 may be a similar effect, as there is some evidence of sub-solar metallicity for this galaxy (e.g., Origlia et al. 2004; Nagao et al. 2011).

Another possible explanation is related to the relatively low gas density observed in M82. In a study of HCN and HCO$^+$ in transitions up to $J = 4 \rightarrow 3$, Jackson et al. (1995) found that the HCN $J = 4 \rightarrow 3/J = 1 \rightarrow 0$ line ratio is significantly smaller for M82 than for NGC 253, both of which are starburst galaxies with intense star formation in galactic nuclei and have comparable IR luminosities. A single-component gas excitation model indicates that the average gas density $n(H_2)$ is at least 10 times lower in M82 ($\sim 10^4$ cm^{-3}) than in NGC 253 ($\sim 5 \times 10^5$ cm^{-3}) (Jackson et al. 1995; Knudsen et al. 2007; Naylor et al. 2010). Compared with the extremely low line ratio of HCN $J = 4 \rightarrow 3/J = 1 \rightarrow 0$ (< 0.1) observed in M82, a factor of more than 10 times lower than in NGC 253, the HCO$^+$ $J = 4 \rightarrow 3/J = 1 \rightarrow 0$ line ratio of M82

also shows a lower value (~ 0.3) than that of NGC 253, but only by a factor of 2-3 (Jackson et al. 1995). Other observations of M82 show that the HCN/HCO$^+$ $J = 3 \rightarrow 2/J = 1 \rightarrow 0$ line ratio is larger than $J = 4 \rightarrow 3/J = 1 \rightarrow 0$ ratio (e.g., Nguyen-Q-Rieu et al. 1989; Wild et al. 1992; Seaquist & Frayer 2000). This may imply a lack of molecular gas with high density, in which case HCO$^+$ is more easily collisionally excited to $J = 4 \rightarrow 3$ than HCN, since the critical density of HCN $J = 4 \rightarrow 3$ ($n_{crit} \sim 5.6 \times 10^6$ cm^{-3}) is higher than that of HCO$^+$ $J = 4 \rightarrow 3$ ($n_{crit} \sim 1.3 \times 10^6$ cm^{-3}) (Meijerink et al. 2007; Yamada et al. 2007; Greve et al. 2009). In addition, studies of chemical complexity toward the nuclear regions of M82 and NGC 253 by molecular line surveys reveal different chemical compositions for these two galaxies (e.g., Martín et al. 2006; Aladro et al. 2011). It is found that the nuclear starburst in M82 represents an evolved state where the heating of molecular clouds is driven by photo-dominated regions (PDRs), while the heating of NGC 253 is dominated by large-scale shocks (Martín et al. 2006). This could be a plausible explanation for the systematic difference of the IR/HCN(4-3) ratio between M82 and NGC 253 that is shown in Fig. 6 (left).

4.5. *Correlations with Warm Dust Temperature*

Fig. 7 shows the $L_{IR}/L'_{HCN(4-3)}$ ratio (left) and the $L_{IR}/L'_{HCO^+(4-3)}$ ratio (right) as a function of $f_{70\mu m}/f_{100\mu m}$ for NGC 253, IC 342, and NGC 6946

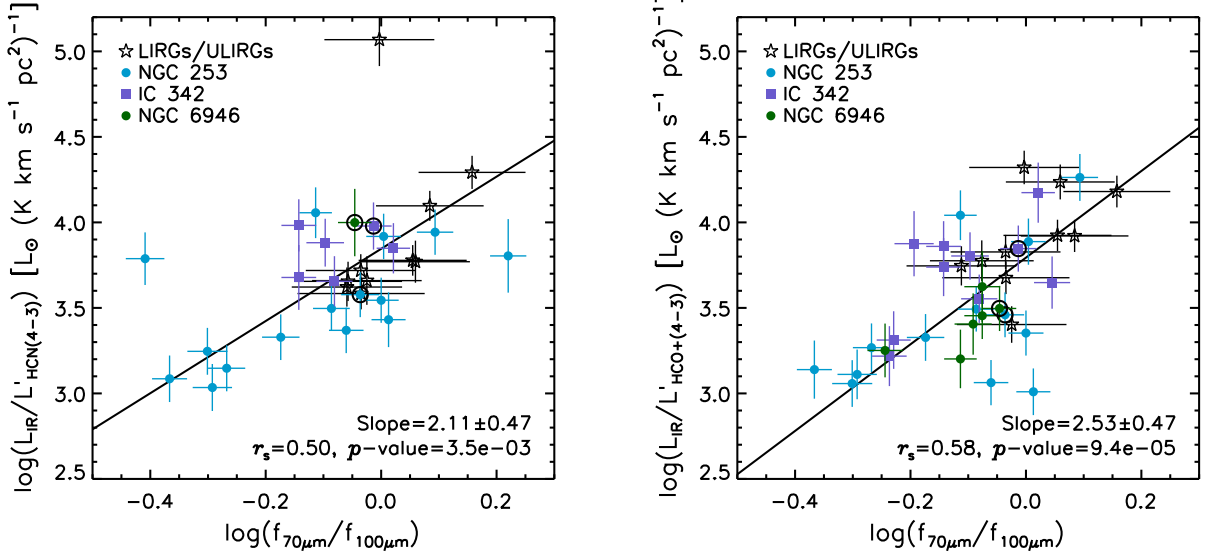**Figure 7.** $L_{\mathrm{IR}}/L'_{\mathrm{HCN}(4-3)}$ (left panel) and $L_{\mathrm{IR}}/L'_{\mathrm{HCO^+(4-3)}}$ (right panel) as a function of 70/100 μm flux ratio for the galaxies in our sample where we have both PACS 70 μm and 100 μm data. The galaxy centers are highlighted with a black circle. The best-fit power-law index and the Spearman rank correlation coefficient for each panel are listed in the bottom right.

where we have both PACS 70 μm and 100 μm data. We adopt the PACS 70/100 μm flux ratio as a proxy for warm-dust temperature, similar to the IRAS 60/100 μm color which is often used to estimate the temperature of the warm-dust component ($T_{\mathrm{d}} \sim 25 - 60$ K; e.g., Solomon et al. 1997; Chanial et al. 2007). We also include a sample of local (U)LIRGs with PACS data from Chu et al. (2017) for comparison. A least-squares fit and a Spearman test yield $\log(L_{\mathrm{IR}}/L'_{\mathrm{HCN}(4-3)}) = 2.1(\pm 0.5)$ $\log(f_{70}/f_{100}) + 3.8$ ($r_{\mathrm{s}} = 0.50$, p-value=3.5×10^{-3}) and $\log(L_{\mathrm{IR}}/L'_{\mathrm{HCO^+(4-3)}}) = 2.5(\pm 0.5) \log(f_{70}/f_{100}) + 3.8$ ($r_{\mathrm{s}} = 0.58$, p-value=9.4×10^{-5}) respectively, indicating that there is a statistically significant correlation between $L_{\mathrm{IR}}/L'_{\mathrm{dense}}$ and T_{d}. These correlations are slightly stronger than the correlation between $L_{\mathrm{IR}}/L'_{\mathrm{HCN}(1-0)}$ and $f_{60\mu m}/f_{100\mu m}$, but not as strong as $L_{\mathrm{IR}}/L'_{\mathrm{CO}(1-0)}$ versus $f_{60\mu m}/f_{100\mu m}$ correlation (correlation coefficient of 0.85; see Fig. 9 in Gao & Solomon 2004b; Liu et al. 2015b).

Comparing the $L_{\mathrm{IR}}/L'_{\mathrm{dense}} - f_{70\mu m}/f_{100\mu m}$ relation with the $L_{\mathrm{IR}}/L'_{\mathrm{dense}} - L_{\mathrm{IR}}$ relation for the individual galaxies, spatially resolved at sub-kpc scales shown in Fig. 6, we find that the ratio of $L_{\mathrm{IR}}/L'_{\mathrm{dense}}$ correlates with both the dust temperature indicated by the observed 70/100 μm flux ratio and the IR luminosity. We speculate that the rising trend of $L_{\mathrm{IR}}/L'_{\mathrm{dense}}$ with L_{IR} observed is likely driven primarily by or related to the correlation of $L_{\mathrm{IR}}/L'_{\mathrm{dense}}$ with T_{d}, since the IR emission from dust grains depends closely on the dust temperature.

4.6. Correlations Between SFE and Dense Gas Fraction

Fig. 8 shows the SFE of the dense molecular gas ($\mathrm{SFE}_{\mathrm{dense}} \equiv \mathrm{SFR}/M_{\mathrm{dense}}$) as a function of the dense-molecular-gas fraction (f_{dense}). The dense-gas content is traced by the HCN $J = 4 \to 3$ (top panel) and the HCO$^+$ $J = 4 \to 3$ (bottom panel) lines, respectively. The SFR is estimated from the total IR luminosity based on the calibrations of Kennicutt (1998) and Murphy et al. (2011):

$$\left(\frac{\mathrm{SFR}}{M_\odot \ \mathrm{yr}^{-1}}\right) = 1.50 \times 10^{-10} \left(\frac{L_{\mathrm{IR}}}{L_\odot}\right). \qquad (7)$$

The SFR is calculated based on a Kroupa (2001) IMF. To better compare with previous work which focuses mostly on the luminosity ratio of HCN/CO at $J = 1 \to 0$ as a measure of the dense-gas fraction (e.g., Gao & Solomon 2004b; Usero et al. 2015), we convert the $J = 4 \to 3$ line luminosity of HCN and HCO$^+$ to the dense-gas mass, and the CO $J = 1 \to 0$ luminosity to the total molecular-gas mass, by assuming conversion factors[6] of α_{dense} and α_{CO}, respectively. We initially assume a Galactic α_{CO} of 4.3 for the full sample of galaxies (Bolatto et al. 2013) (left column).

The mass of dense molecular gas can be estimated from $L'_{\mathrm{HCN}(4-3)}$ and $L'_{\mathrm{HCO^+(4-3)}}$,

$$M_{\mathrm{dense}} = \alpha_{\mathrm{dense}} \left(\frac{L'_{\mathrm{gas} \ J=4-3}}{r_{41}}\right), \qquad (8)$$

---

[6] The units of the luminosity-to-mass conversion factor, $M_\odot$ (K km s^{-1} pc^2)$^{-1}$, are omitted from the text for brevity.

where $\alpha_{\rm dense}$ is the HCN(HCO$^+$) $J = 1 \to 0$-to-dense-gas-mass conversion factor and r_{41} is the HCN(HCO$^+$) $J = 4 \to 3/\ J = 1 \to 0$ line ratio. For simplicity, we assume a fixed $\alpha_{\rm dense} = 10$ for both HCN $J = 1 \to 0$ and HCO$^+$ $J = 1 \to 0$ emission, which was estimated by Gao & Solomon (2004b) for normal SF galaxies with a brightness temperature of $T_{\rm b} = 35$ K. We adopt $r_{41} = 0.3$, which is an average ratio estimated by comparing the HCN $J = 4 \to 3$ data of Zhang et al. (2014) (including the data presented in this study) with the HCN $J = 1 \to 0$ data of Gao & Solomon (2004a). Note that the r_{41} we used is a rough estimate with large uncertainty partly due to the slightly different angular resolution of the HCN $J = 4 \to 3$ and the HCN $J = 1 \to 0$ observations. Also note that the dense-gas mass of extreme systems, i.e., galaxies or regions that are more excited in molecular gas emission with higher gas temperature, is likely overestimated under the assumption of a fixed r_{41}. The HCN $J = 4 \to 3$ observations of a few (U)LIRGs indeed show higher r_{41} ranging from ~ 0.3 to 1.0 (Papadopoulos 2007).

We adopt here the assumption that the $L_{\rm IR}/L'_{\rm HCN(4-3)}$ ratio is a proxy for the SFE of the dense gas (SFE$_{\rm dense} \propto L_{\rm IR}/L'_{\rm HCN(4-3)}$), assuming that both the $\alpha_{\rm dense}$ and the line ratio r_{41} are constant for the full sample of galaxies. Similar assumptions are applied to the dense gas as traced by the HCO$^+$ $J = 4 \to 3$ line. A Spearman test yields a statistically insignificant correlation with $r_{\rm s} = -0.36$ and a p-value of 0.0053 for HCN $J = 4 \to 3$ and with $r_{\rm s} = -0.04$ and a p-value of 0.718 for HCO$^+$ $J = 4 \to 3$, indicating a very weak dependence, if any, between SFE$_{\rm dense}$ and $f_{\rm dense}$ within our sample. It is clearly illustrated in Fig. 8 that the fraction of dense gas is higher in starbursts and galactic centers (*circled point*) than in the outer regions of our sample galaxies, although there are some off-nuclear positions that have similar $f_{\rm dense}$ as the central region (e.g., M82). These are in good agreement with previous HCN $J = 1 \to 0$ studies and confirm the findings by Gao & Solomon (2004a,b) that the starburst strength can be better indicated by the fraction of molecular gas in dense phase. For the nearby normal, star-forming galaxies, the mean $\log(f_{\rm dense})$ are -0.89±0.07 and -0.98±0.04, with an rms scatter of 0.28 dex and 0.22 dex, for the dense gas as traced by HCN $J = 4 \to 3$ and HCO$^+$ $J = 4 \to 3$, respectively. The small scatter in these ratios indicates that the dense-gas fraction varies little for galaxies with normal star formation activity, which seems to be a plausible explanation for the linear relation found between $\Sigma_{\rm SFR}$ and $\Sigma_{\rm gas}$ in nearby normal galaxies (e.g., Bigiel et al. 2008; Lada et al. 2012).

It is evident from Fig. 8(left) that one of high-z quasars in our sample exhibits excess dense-gas content with an unphysical dense-gas fraction ($f_{\rm dense} > 1$), if we adopt a Galactic $\alpha_{\rm CO}$ and $\alpha_{\rm dense}$. Observations of luminous IR galaxies show that molecular clouds in starbursts are highly concentrated with large velocity dispersions and have higher average gas volume densities than a typical GMC in the Milky Way (Bolatto et al. 2013, and references therein), implying that a smaller $\alpha_{\rm CO}$ is more appropriate for these galaxies (e.g., Leroy et al. 2015a,b). Note that the molecular-gas mass measured for the central nuclear regions of star-forming galaxies may be overestimated for a Galactic $\alpha_{\rm CO}$ (Sandstrom et al. 2013). It is expected that the CO-to-H$_2$ conversion factor has a dependence on the physical conditions in the molecular clouds, $\alpha_{\rm CO} \propto \rho^{0.5}/T_{\rm b}$, if we assume the emission orginates in the gravitationally bound and virialized cloud cores (e.g., Bolatto et al. 2013). The multiline analysis of HCN and HCO$^+$ by Graciá-Carpio et al. (2008) presents evidence that $\alpha_{\rm HCN}$ is probably about three times lower in IR luminous galaxies. The potential variation of the dense-gas excitation (e.g., HCN $J = 4 \to 3/J = 1 \to 0$ line ratio) in different physical conditions could also play an important role in estimating the dense-gas content.

With these results we assume a ULIRG-like $\alpha_{\rm CO}$=0.8, and $\alpha_{\rm dense} = \alpha_{\rm dense}^{\rm MW}/3.2$ for the dense gas as traced by the HCN and the HCO$^+$ emission in extreme starbursts (NGC 253, M82, (U)LIRGs, and high-z quasars), similar to the value adopted for LIRGs/ULIRGs in García-Burillo et al. (2012). For comparison, in Fig. 8 (right) we also plot the data points for starbursts by assuming a revised $\alpha_{\rm CO}$ and $\alpha_{\rm dense}$, while keep using Galactic conversion factors for the remaining normal disk galaxies. A Spearman test to the data of extreme starbursts with gas content calculated with the revised $\alpha_{\rm CO}$ and $\alpha_{\rm dense}$ combined with normal disk galaxies, gives similar correlation coefficients ($r_{\rm s} = -0.04$ and p-value = 0.79 for HCN $J = 4 \to 3$, $r_{\rm s} = 0.42$ and p-value = 2.1×10^{-4} for HCO$^+$ $J = 4 \to 3$) as the results derived based on the assumption of fixed conversion factors. The weak correlation revealed suggests that the efficiency of star formation in the dense gas is likely to be independent of dense-gas fraction. Keeping in mind the dependency revealed for $L_{\rm IR}/L'_{\rm dense}$ ratio with warm dust temperature shown in Sect. 4.5, we note that the uncertainties of conversion factors ($\alpha_{\rm CO}$ and $\alpha_{\rm dense}$) may introduce some biases in interpreting the correlations between the SFE of dense gas and the dense gas fraction.

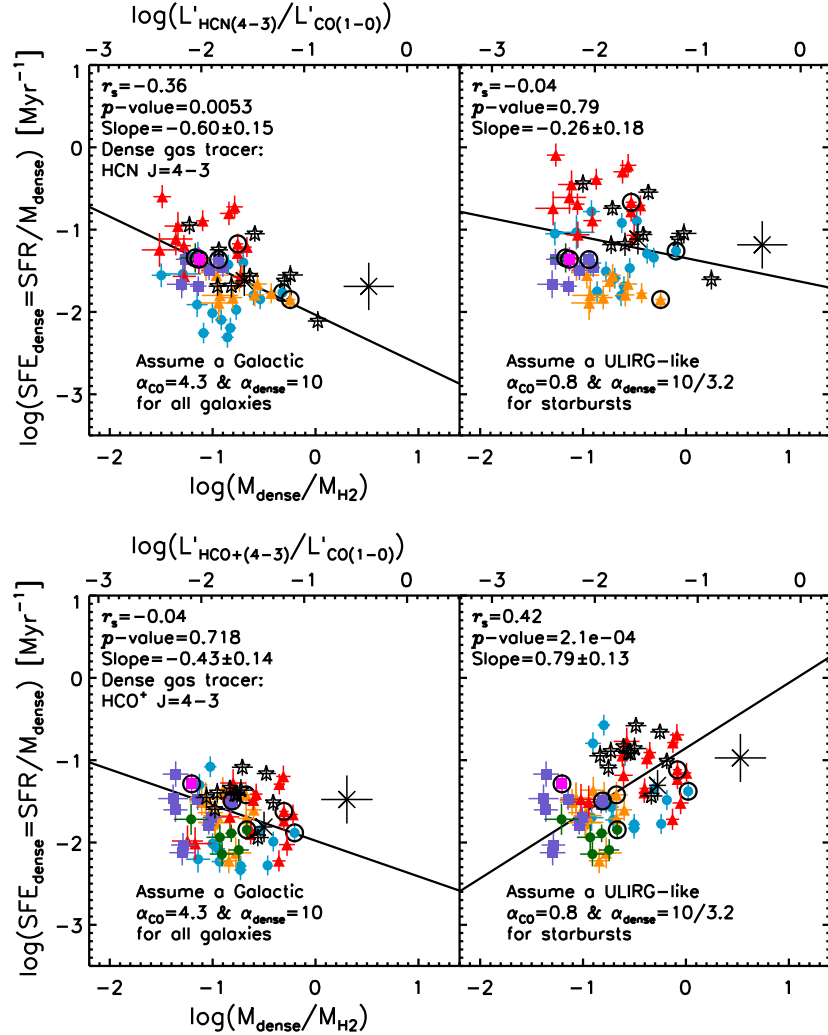We also plot the SFE of the total molecular gas, i.e., the inverse of the molecular-gas depletion time ($\tau_{\rm gas}$),

Figure 8. SFE of the dense molecular gas as a function of the dense-gas fraction, with dense gas as traced by the HCN $J = 4 \to 3$ (top row) and the HCO$^+$ $J = 4 \to 3$ (bottom row) lines for the sample of galaxies compiled in this work. The left panels show the data that assume a Galactic $\alpha_{\rm CO}$ of 4.3 and $\alpha_{\rm dense}$ of 10 for the full sample of galaxies, while the right panels represent the data that adopt a ULIRG-like $\alpha_{\rm CO}$ of 0.8 and $\alpha_{\rm dense}$ of 10/3.2 for starbursts (NGC 253, M82, (U)LIRGs, and high-z quasars). We assume a fixed $\alpha_{\rm dense}$ and line brightness temperature ratio r_{41} to estimate the mass of molecular gas in the dense phase for the full sample of galaxies. Symbols are as in Fig. 5. The data points highlighted with a black circle denote the central position of each galaxy. The Spearman rank correlation coefficient for each panel is listed in the top left.

as a function of $f_{\rm dense}$ (see Fig. 9). These are similar to the relations shown in Fig. 5 (top), but we convert the IR and line luminosities to SFR and gas mass, respectively. Similar as in Fig. 8, we assume Galactic and ULIRG-like conversion factors for the starbursts in our sample for comparison, respectively. It is clearly that the SFE$_{\rm mol}$ increases with $f_{\rm dense}$ with a strong correlation coefficient ($r_{\rm s} \sim 0.6$ with p-value $<10^{-6}$ for HCN $J = 4 \to 3$ and $r_{\rm s} \sim 0.7 - 0.8$ with p-value $<10^{-10}$ for HCO$^+$ $J = 4 \to 3$). While a nearly constant SFE$_{\rm mol}$ is found for normal star-forming galaxy disks by Usero et al. (2015), our data show that the SFE$_{\rm mol}$ is strongly correlated with $f_{\rm dense}$ when combining normal

disks with more extreme luminous IR galaxies. Here we also note the large uncertainties involved in the derivation of correlations, due to the limited data points and the effect of correlated axes, as well as the assumption of conversion factors.

Compared with the normal galaxies, the higher SFE found in (U)LIRGs and the high-z quasars indicates that the latter will consume their total gas reservoir more quickly. This is consistent with the trend seen between $\tau_{\rm gas}$ and $L_{\rm FIR}$ where the depletion timescale is typically one order of magnitude shorter for ULIRGs and high-z quasars with higher $L_{\rm FIR}$ than for normal spiral galaxies (e.g., Solomon & Vanden Bout 2005; Daddi et al. 2010;
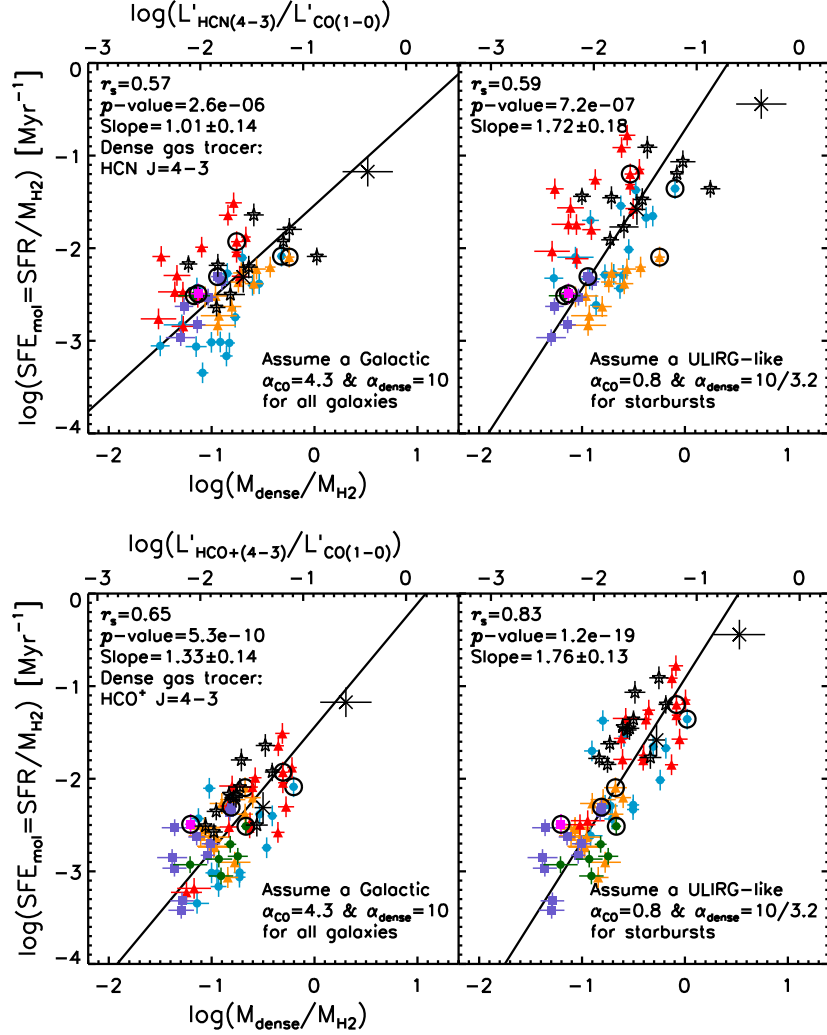
Figure 9. Similar to Fig. 8, but we plot the SFE of the total molecular gas as a function of the dense-gas fraction.

Combes et al. 2013; Carilli & Walter 2013). As expected, the galaxy centers tend to show higher SFE_{mol} than the outer regions as a result of the starburst environment in the galactic nuclear region.

5. THE HCN(4−3) TO HCO$^+$(4−3) LINE RATIO

In Fig. 10 (left), we plot the HCN to HCO$^+$ $J = 4 \rightarrow 3$ luminosity ratio as a function of IR luminosity for our target galaxies combining measurements of normal spirals, (U)LIRGs, and quasars from the literature to inspect the variation of the HCN/HCO$^+$ line ratio. It is apparent that no systematic trend is found between L'_{HCN}/L'_{HCO^+} and L_{IR}. The L'_{HCN}/L'_{HCO^+} $J = 4 \rightarrow 3$ ratio varies from 0.1 to 2.7 with a mean value of 0.9 and an rms scatter of 0.6 for the targeted six galaxies, while an average ratio of 0.8±0.5 is found for normal star-forming galaxies without AGN embedded. The L'_{HCN}/L'_{HCO^+} $J = 4 \rightarrow 3$ ratio varies from 0.1 to 3.0 for the full sample of galaxies, in agree-

ment with the HCN/HCO$^+$ luminosity ratios observed at $J = 1 \rightarrow 0$ and $J = 3 \rightarrow 2$ transitions (e.g., Imanishi et al. 2016; Privon et al. 2015; Knudsen et al. 2007; Krips et al. 2008).

The lowest HCN/HCO$^+$ line ratios in our sample are found in M82 and appear to be constant across the starburst disk with a mean value of ~ 0.3, which is consistent with previous JCMT observations of M82 (Seaquist & Frayer 2000). As discussed in Sect. 4.4, we consider that the low HCN/HCO$^+$ ratio observed in M82 is more likely due to a deficit of HCN, rather than an increase of HCO$^+$, given that HCN is much weaker than HCO$^+$ with respect to the IR emission (see Fig. 6). Moreover, we speculate that the weakness of HCN in M82 could be attributed to the decrease of nitrogen abundance in the sub-solar metallicity environment and/or the relatively low gas density condition of this galaxy. For NGC 3628 and NGC 6946, which show
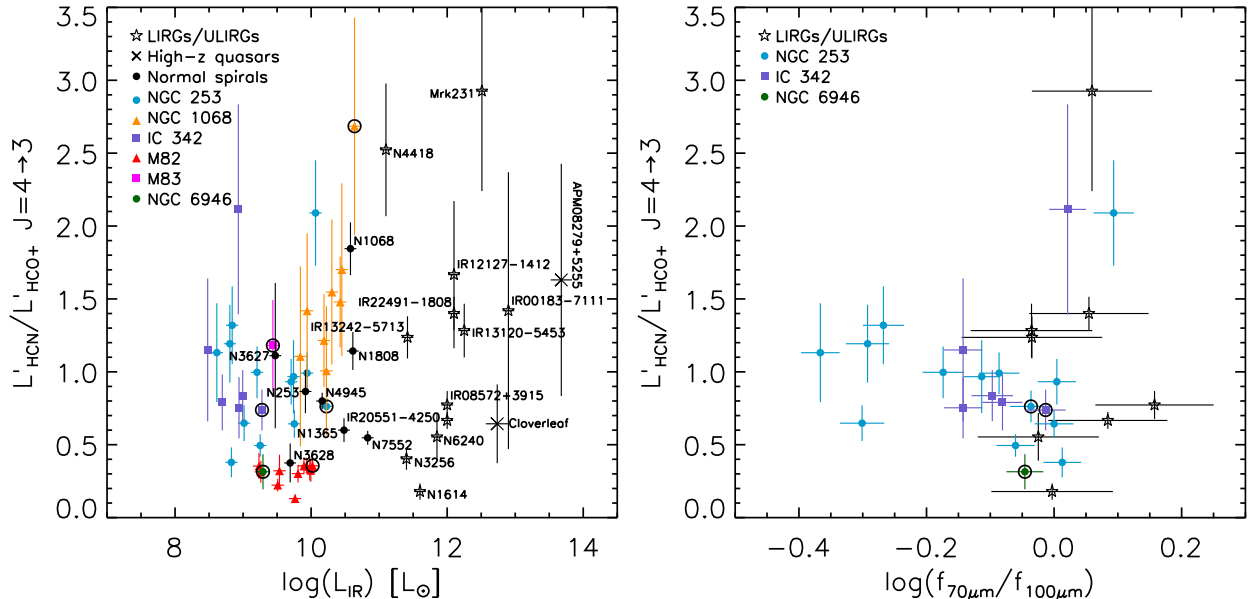
Figure 10. HCN/HCO$^+$ $J = 4 \rightarrow 3$ luminosity ratio as a function of IR luminosity (left panel) and 70 μm/100 μm flux ratio (right panel) for our sample of galaxies that are spatially resolved (*colored symbols*), and the normal galaxies (*solid circles*), local (U)LIRGs (*open stars*), and high-z quasars (*crosses*) from the literature. The galaxy centers of the six targeted galaxies are highlighted with black circles.

comparably low HCN/HCO$^+$ ratios in Fig. 10 (left), it has been found that their metallicities are sub-solar (Engelbracht et al. 2008; Gazak et al. 2014). In addition, NGC 3256 and NGC 1614 also show relatively low HCN/HCO$^+$ ratios (≤ 0.4, see Fig. 10 (left)). Weak HCN $J = 1 \rightarrow 0$ emission and a relatively low HCN/HCO$^+$ $J = 1 \rightarrow 0$ ratio for NGC 1614 have also been reported by García-Burillo et al. (2012). We speculate that the weakness of HCN in these two galaxies may be related to the deficiency of high-density gas, since both galaxies are merger remnants at an advanced merger stage that probably have dispersed their molecular gas by shocks from supernova explosions (e.g., Jackson et al. 1995; Costagliola et al. 2011).

An enhancement of the HCN/HCO$^+$ abundance ratio in X-ray-dominated regions with modest densities ($n < 10^4 - 10^5$ cm^{-3}) is predicted by theoretical models (e.g., Lepp & Dalgarno 1996; Meijerink et al. 2007). Observations show evidence for HCN enhancement in nearby galaxies hosting AGNs (e.g., Kohno et al. 2001; Krips et al. 2008; Izumi et al. 2016). We see from Fig. 10 (left) that the Seyfert 2 galaxy NGC 1068 shows a high HCN/HCO$^+$ ratio with the highest value in the center, in contrast to the low ratio observed in the pure starburst, such as in M82. High HCN/HCO$^+$ line ratios are also found in NGC 4418 and Mrk 231, which could be associated with the enhancement of HCN by X-ray radiation from the AGN. The HCN and HCO$^+$ $J = 1 \rightarrow 0$ observations also show relatively

high line ratios for these galaxies (e.g., Imanishi et al. 2004; Costagliola et al. 2011). However, for the Cloverleaf, which is a high-z quasar hosting AGN, a similar enhancement of HCN is not found. Instead, a relatively low HCN/HCO$^+$ ratio that is comparable to starburst-dominated systems is obtained for this galaxy. It has been argued that the variation of the HCN/HCO$^+$ ratio is likely determined by multiple processes including the interplay of radiation field and gas density (e.g., Papadopoulos 2007; Harada et al. 2010, 2013; Privon et al. 2015).

We also examine the relationship between the HCN/HCO$^+$ $J = 4 \rightarrow 3$ line ratio and the $f_{70\mu m}/f_{100\mu m}$ flux ratio for the galaxies where we have both PACS 70 μm and 100 μm data (see Fig. 10 (right)). No significant correlation is found between HCN/HCO$^+$ and 70/100 μm color temperature. A study of the excitation mechanisms for HCN and HCO$^+$ emission which includes low-J observations will be presented in a future paper.

6. SUMMARY

We have presented observations of the HCN $J = 4 \rightarrow 3$ and the HCO$^+$ $J = 4 \rightarrow 3$ lines in the central $\sim 50'' \times 50''$ regions of six nearby star-forming galaxies from the JCMT program MALATANG. We combined these new data with previous multi-wavelength observations to study the relationships between the dense molecular gas as traced by the $J = 4 \rightarrow 3$ lines of HCN and HCO$^+$, the IR luminosity, and the dust and star-

formation properties. Finally, we discussed the variation of the HCN/HCO$^+$ $J = 4 \to 3$ line ratio in different populations of galaxies. We summarize below the main results and conclusions of this work.

1. We detect HCN and HCO$^+$ $J = 4 \to 3$ emission in all six targeted galaxies at multiple positions except for M83 where only weak detections at the central position were obtained. Both the line profiles and line widths are found to be very similar for HCN and HCO$^+$, indicating that these two molecules are arising from the same region.

2. All galaxies observed in our sample are spatially resolved at sub-kpc scales and follow the linear relation of $L_{IR} - L'_{dense}$ (dense gas as traced by HCN and HCO$^+$ $J = 4 \to 3$) established globally in galaxies within the scatter. Our new data extend the relation to an intermediate luminosity regime to bridge the gap between Galactic clumps and integrated galaxies. The nearly linear slopes obtained for the $L_{IR} - L'_{HCN(4-3)}$ and $L_{IR} - L'_{HCO^+(4-3)}$ relations are inconsistent with the sub-linear relations predicted by some theoretical models.

3. We find that the L_{IR}/L'_{dense} ratio shows a systematic trend with L_{IR} within individual galaxies, whereas the galaxy-integrated ratios vary little. Similar trends are also found between the L_{IR}/L_{gas} ratio and the warm-dust temperature gauged by the $70/100$ μm flux ratio.

4. Using appropriate conversion factors of α_{CO} and α_{dense} for normal star-forming galaxies, local (U)LIRGs, and high-z quasars, we find the fraction of dense gas is higher in (U)LIRGs, high-z quasars, and galactic centers than in the outer regions of our sample galaxies where a small variation of dense-gas fraction is found. The SFE of the dense molecular gas appears to be nearly independent of dense-gas fraction for our sample of galaxies, while the SFE of the total molecular gas increases substantially with dense-gas fraction when combining our data with local (U)LIRGs and high-z quasars.

5. The HCN/HCO$^+$ $J = 4 \to 3$ ratio varies from 0.1 to 2.7 with a mean value of 0.9 and an rms scatter of 0.6 for the targeted six galaxies. No obvious correlation is found between HCN/HCO$^+$ line ratio and either IR luminosity or warm-dust temperature. We speculate that the low HCN/HCO$^+$ $J = 4 \to 3$ ratio found in M82 could be attributed to either a low HCN abundance and/or lack of gas with high enough density to excite the HCN $J = 4 \to 3$ emission in this galaxy. The highest ratios are found in AGN-dominated systems, consistent with a scenario in which the presence of an AGN could cause an enhancement of the HCN abundance.
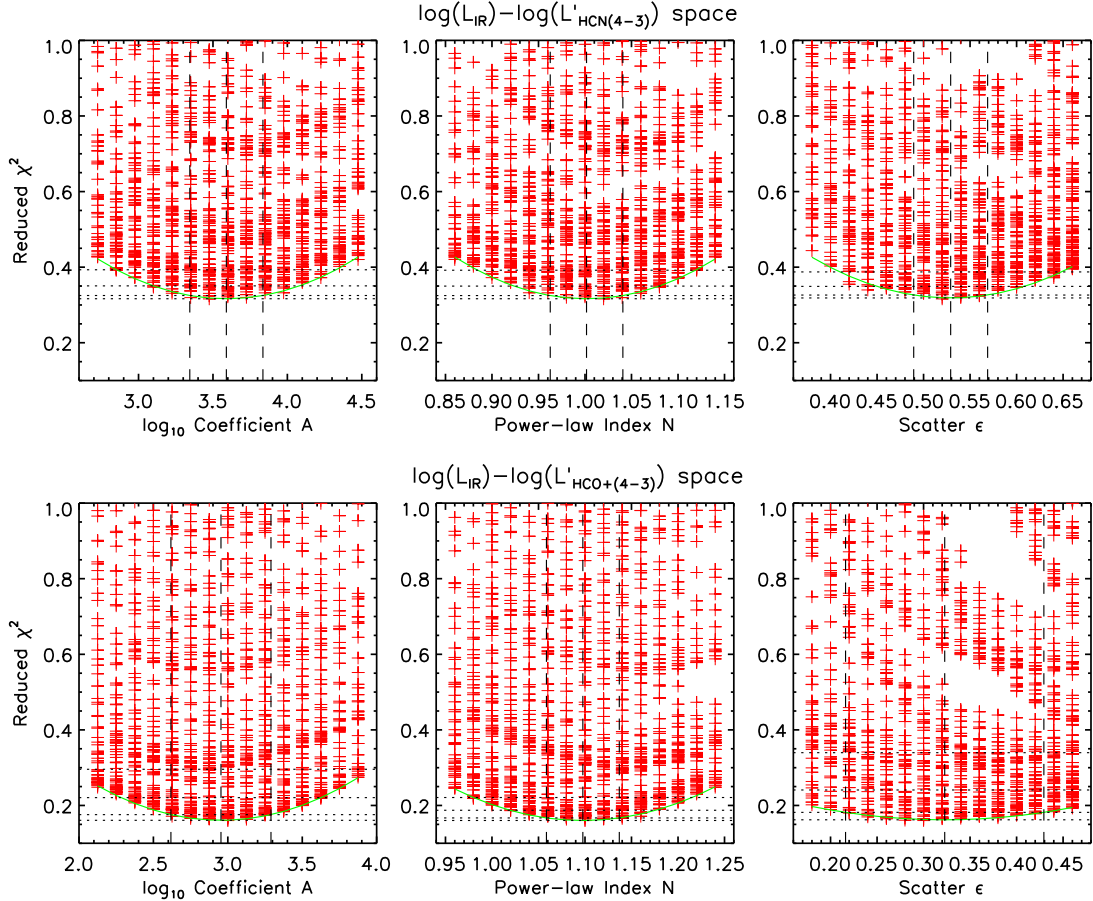
Figure 11. Reduced χ^2 for the three parameters $\{A, N, \epsilon\}$ in the MC fitting of $L_{\rm IR} - L'_{\rm HCN(4-3)}$ relation (top row) and $L_{\rm IR} - L'_{\rm HCO^+(4-3)}$ relation (bottom row) , marginalized over the other two. Red crosses show the χ^2 obtained for each sampled combination of parameters. The best-fit χ^2 is obtained by fitting a quadratic function to the minimum χ^2 at each parameter value sampled. The best-fit quadratic function is shown in green line and the best-fit χ^2 together with the $1\,\sigma$, $2\,\sigma$, and $3\,\sigma$ levels are shown as horizontal dotted lines. The vertical dashed lines represent the best-fit parameter and its $1\,\sigma$ uncertainty which is estimated by a bootstrapping method.

APPENDIX

A. THE FITTING METHOD USING A MONTE CARLO APPROACH

Based on Blanc et al. (2009) and Leroy et al. (2013), we fit the data using a Monte Carlo approach which allows us to include upper limits in the fit and incorporate the intrinsic scatter in the $L_{\rm IR} - L'_{\rm dense}$ relation as a free parameter. In the following, we describe this approach.

1. We generate 1000 MC realizations of the data for each set of parameters $\{A, N, \epsilon\}$. For each realization, we take the observed $L'_{\rm dense}$ as the true value and calculate the corresponding true $L_{\rm IR}$ using Equation (6), drawing a new value from $\mathcal{N}(0, \epsilon)$ for each data point to introduce the intrinsic scatter. We apply the observational uncertainties in $L'_{\rm gas}$ and $L_{\rm IR}$ by offseting the data points by random amounts. The uncertainty in $L'_{\rm dense}$ is derived from statistical measurement errors and the systematic uncertainties in flux calibration (see Sect. 2.1), while the uncertainty in $L_{\rm IR}$ includes the statistical measurement errors and the errors introduced by the flux calibration and the TIR calibration from combined luminosities (see Section 3.3). For the non-detection of HCN $J = 4 \rightarrow 3$ and HCO$^+$ $J = 4 \rightarrow 3$ emission, we use the measured values of these data points together with their error bars in the fitting procedure and exclude data with velocity-integrated intensity $I_{\rm dense} \leq 0$, given that our data are mainly limited by the sensitivity of the dense-gas observations.
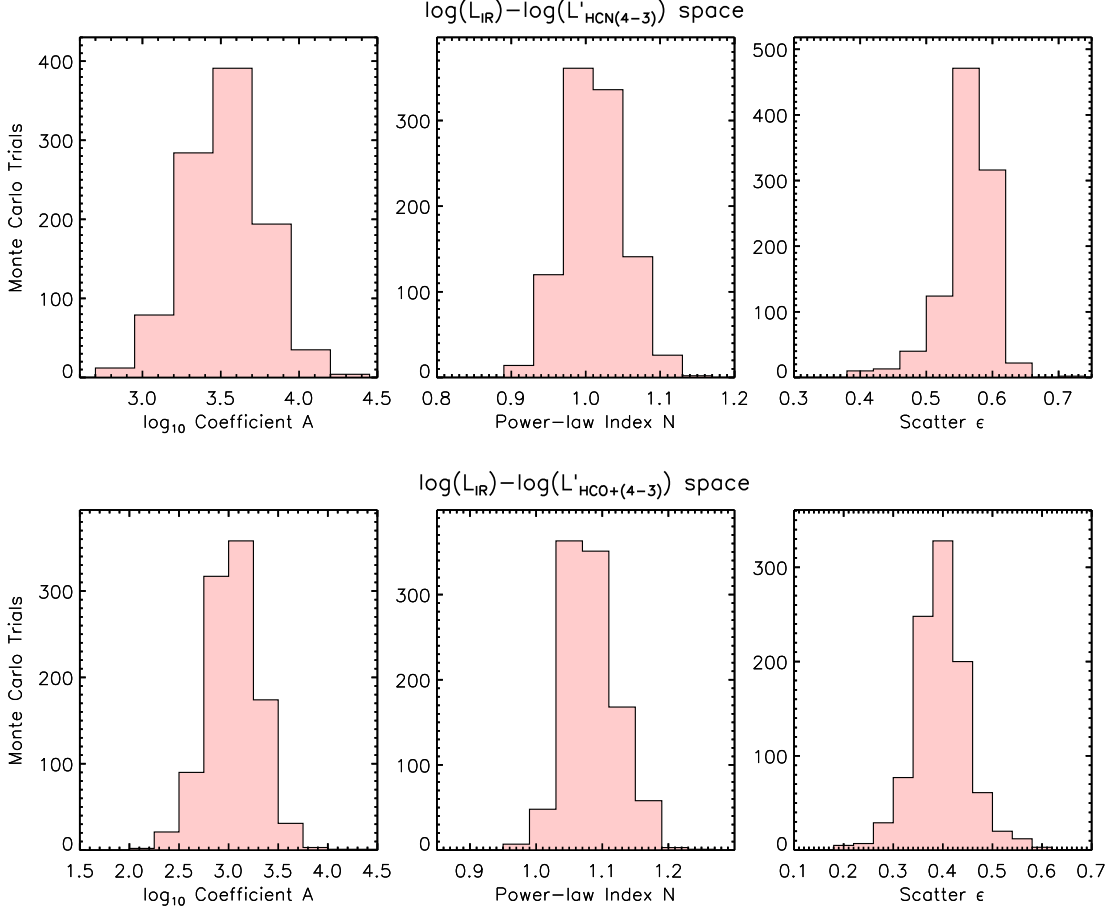
Figure 12. Distribution of the best-fit parameters $\{A, N, \epsilon\}$ for the 1000 bootstrapping iterations to estimate the uncertainty for the parameters we determined based on the MC fitting to the $L_{\rm IR} - L'_{\rm HCN(4-3)}$ relation (top row) and the $L_{\rm IR} - L'_{\rm HCO+(4-3)}$ relation (bottom row).

2. We grid our observed data in $\log_{10} L_{\rm IR} - \log_{10} L'_{\rm dense}$ space using cells 0.75 dex wide in both dimensions. We then compare the distribution of the gridded data with the model data from the MC realizations in the $\log_{10} L_{\rm IR} - \log_{10} L'_{\rm dense}$ plane by counting the number of data points falling in each cell for each combination of $\{A, N, \epsilon\}$. After renormalizing the MC grid to have the same amount of data as the observed grid, we calculate a goodness-of-fit estimate which is referred to as χ^2 following Blanc et al. (2009):

$$\chi^2 = \sum_i \frac{(N^i_{\rm obs} - N^i_{\rm model})^2}{N^i_{\rm model}} \tag{A1}$$

where the sum is over all grid cells, and $N^i_{\rm obs}$ and $N^i_{\rm model}$ are the number of observed and model data points respectively in grid cell i.

3. We take a bootstrapping approach to estimate the errors in the parameters $\{A, N, \epsilon\}$ by randomly re-sampling the data points in each grid cell and performing the above MC analysis. The bootstrap procedure is repeated 1000 times for each solution and we measure the resulting standard deviation of the parameter values $\{A, N, \epsilon\}$.

Figure 11 shows the reduced χ^2 for the three parameters $\{A, N, \epsilon\}$ in the fit, marginalized over the other two. Similar to Figure 14 of Blanc et al. (2009), the best-fit value for each parameter is obtained by fitting a quadratic function to the minimum χ^2 for each parameter value sampled. We adopt the 1 σ dispersion of the χ^2 distributions obtained through a bootstrapping approach for the estimate of the uncertainty in the parameters $\{A, N, \epsilon\}$ (see Fig. 12).

REFERENCES

Aalto, S., Booth, R. S., Black, J. H., & Johansson, L. E. B. 1995, A&A, 300, 369

Aalto, S., Garcia-Burillo, S., Muller, S., et al. 2012, A&A, 537, A44

Aalto, S., Martín, S., Costagliola, F., et al. 2015, A&A, 584, A42

Aladro, R., Martín, S., Martín-Pintado, J., et al. 2011, A&A, 535, A84

Aniano, G., Draine, B. T., Gordon, K. D., & Sandstrom, K. 2011, PASP, 123, 1218

Baan, W. A., Henkel, C., Loenen, A. F., Baudry, A., & Wiklind, T. 2008, A&A, 477, 747

Balog, Z., Müller, T., Nielbock, M., et al. 2014, Experimental Astronomy, 37, 129

Barvainis, R., Maloney, P., Antonucci, R., & Alloin, D. 1997, ApJ, 484, 695

Bayet, E., Davis, T. A., Bell, T. A., & Viti, S. 2012, MNRAS, 424, 2646

Bigiel, F., Leroy, A., Walter, F., et al. 2008, AJ, 136, 2846

Bigiel, F., Leroy, A. K., Blitz, L., et al. 2015, ApJ, 815, 103

Bigiel, F., Leroy, A. K., Jiménez-Donaire, M. J., et al. 2016, ApJL, 822, L26

Blanc, G. A., Heiderman, A., Gebhardt, K., Evans, II, N. J., & Adams, J. 2009, ApJ, 704, 842

Bolatto, A. D., Wolfire, M., & Leroy, A. K. 2013, ARA&A, 51, 207

Braine, J., Shimajiri, Y., André, P., et al. 2017, A&A, 597, A44

Buckle, J. V., Hills, R. E., Smith, H., et al. 2009, MNRAS, 399, 1026

Bussmann, R. S., Narayanan, D., Shirley, Y. L., et al. 2008, ApJL, 681, L73

Carilli, C. L., & Walter, F. 2013, ARA&A, 51, 105

Chanial, P., Flores, H., Guiderdoni, B., et al. 2007, A&A, 462, 81

Chen, H., Braine, J., Gao, Y., Koda, J., & Gu, Q. 2017, ApJ, 836, 101

Chen, H., Gao, Y., Braine, J., & Gu, Q. 2015, ApJ, 810, 140

Chu, J. K., Sanders, D. B., Larson, K. L., et al. 2017, ApJS, 229, 25

Combes, F., García-Burillo, S., Braine, J., et al. 2013, A&A, 550, A41

Costagliola, F., Aalto, S., Rodriguez, M. I., et al. 2011, A&A, 528, A30

Daddi, E., Elbaz, D., Walter, F., et al. 2010, ApJL, 714, L118

Dalcanton, J. J., Williams, B. F., Seth, A. C., et al. 2009, ApJS, 183, 67

Davis, T. A., Bayet, E., Crocker, A., Topal, S., & Bureau, M. 2013, MNRAS, 433, 1659

Elmegreen, B. G. 2015, ApJL, 814, L30

—. 2018, ApJ, 854, 16

Engelbracht, C. W., Rieke, G. H., Gordon, K. D., et al. 2008, ApJ, 678, 804

Evans, II, N. J. 2008, in Astronomical Society of the Pacific Conference Series, Vol. 390, Pathways Through an Eclectic Universe, ed. J. H. Knapen, T. J. Mahoney, & A. Vazdekis, 52

Evans, II, N. J., Heiderman, A., & Vutisalchavakul, N. 2014, ApJ, 782, 114

Galametz, M., Kennicutt, R. C., Calzetti, D., et al. 2013, MNRAS, 431, 1956

Gao, Y. 1996, PhD thesis, STATE UNIVERSITY OF NEW YORK AT STONY BROOK

Gao, Y., Carilli, C. L., Solomon, P. M., & Vanden Bout, P. A. 2007, ApJL, 660, L93

Gao, Y., & Solomon, P. M. 2004a, ApJS, 152, 63

—. 2004b, ApJ, 606, 271

García-Burillo, S., Usero, A., Alonso-Herrero, A., et al. 2012, A&A, 539, A8

García-Burillo, S., Combes, F., Usero, A., et al. 2014, A&A, 567, A125

Gazak, J. Z., Davies, B., Bastian, N., et al. 2014, ApJ, 787, 142

Goldsmith, P. F., & Kauffmann, J. 2017, ApJ, 841, 25

Graciá-Carpio, J., García-Burillo, S., Planesas, P., & Colina, L. 2006, ApJL, 640, L135

Graciá-Carpio, J., García-Burillo, S., Planesas, P., Fuente, A., & Usero, A. 2008, A&A, 479, 703

Greve, T. R., Papadopoulos, P. P., Gao, Y., & Radford, S. J. E. 2009, ApJ, 692, 1432

Greve, T. R., Leonidaki, I., Xilouris, E. M., et al. 2014, ApJ, 794, 142

Harada, N., Herbst, E., & Wakelam, V. 2010, ApJ, 721, 1570

Harada, N., Thompson, T. A., & Herbst, E. 2013, ApJ, 765, 108

Heiderman, A., Evans, II, N. J., Allen, L. E., Huard, T., & Heyer, M. 2010, ApJ, 723, 1019

Helou, G., Soifer, B. T., & Rowan-Robinson, M. 1985, ApJL, 298, L7

Imanishi, M., & Nakanishi, K. 2013a, AJ, 146, 91

—. 2013b, AJ, 146, 47

—. 2014, AJ, 148, 9

Imanishi, M., Nakanishi, K., & Izumi, T. 2016, AJ, 152, 218

Imanishi, M., Nakanishi, K., Kuno, N., & Kohno, K. 2004, AJ, 128, 2037

Izumi, T., Kohno, K., Aalto, S., et al. 2016, ApJ, 818, 42

Jackson, J. M., Paglione, T. A. D., Carlstrom, J. E., & Rieu, N.-Q. 1995, ApJ, 438, 695

Jenness, T., Chapin, E. L., Berry, D. S., et al. 2013, SMURF: SubMillimeter User Reduction Facility, Astrophysics Source Code Library, ascl:1310.007

Jenness, T., Currie, M. J., Tilanus, R. P. J., et al. 2015, MNRAS, 453, 73

Juneau, S., Narayanan, D. T., Moustakas, J., et al. 2009, ApJ, 707, 1217

Kauffmann, J., Goldsmith, P. F., Melnick, G., et al. 2017, A&A, 605, L5

Kelly, B. C. 2007, ApJ, 665, 1489

Kennicutt, R. C., & Evans, N. J. 2012, ARA&A, 50, 531

Kennicutt, R. C., Calzetti, D., Aniano, G., et al. 2011, PASP, 123, 1347

Kennicutt, Jr., R. C. 1998, ApJ, 498, 541

Knudsen, K. K., Walter, F., Weiss, A., et al. 2007, ApJ, 666, 156

Kohno, K., Kawabe, R., Tosaki, T., & Okumura, S. K. 1996, ApJL, 461, L29

Kohno, K., Matsushita, S., Vila-Vilaró, B., et al. 2001, in Astronomical Society of the Pacific Conference Series, Vol. 249, The Central Kiloparsec of Starbursts and AGN: The La Palma Connection, ed. J. H. Knapen, J. E. Beckman, I. Shlosman, & T. J. Mahoney, 672

Krips, M., Neri, R., García-Burillo, S., et al. 2008, ApJ, 677, 262

Krips, M., Martín, S., Eckart, A., et al. 2011, ApJ, 736, 37

Kroupa, P. 2001, MNRAS, 322, 231

Krumholz, M. R., & McKee, C. F. 2005, ApJ, 630, 250

Krumholz, M. R., & Thompson, T. A. 2007, ApJ, 669, 289

Kuno, N., Sato, N., Nakanishi, H., et al. 2007, PASJ, 59, 117

Lada, C. J., Forbrich, J., Lombardi, M., & Alves, J. F. 2012, ApJ, 745, 190

Lada, C. J., Lombardi, M., & Alves, J. F. 2010, ApJ, 724, 687

Lepp, S., & Dalgarno, A. 1996, A&A, 306, L21

Leroy, A. K., Walter, F., Brinks, E., et al. 2008, AJ, 136, 2782

Leroy, A. K., Walter, F., Sandstrom, K., et al. 2013, AJ, 146, 19

Leroy, A. K., Bolatto, A. D., Ostriker, E. C., et al. 2015a, ApJ, 801, 25

Leroy, A. K., Walter, F., Martini, P., et al. 2015b, ApJ, 814, 83

Liu, D., Gao, Y., Isaak, K., et al. 2015a, ApJL, 810, L14

Liu, F., & Gao, Y. 2010, ApJ, 713, 524

Liu, L., Gao, Y., & Greve, T. R. 2015b, ApJ, 805, 31

Liu, T., Kim, K.-T., Yoo, H., et al. 2016, ApJ, 829, 59

Lu, N., Zhao, Y., Xu, C. K., et al. 2014, ApJL, 787, L23

Mao, R.-Q., Schulz, A., Henkel, C., et al. 2010, ApJ, 724, 1336

Markwardt, C. B. 2009, in Astronomical Society of the Pacific Conference Series, Vol. 411, Astronomical Data Analysis Software and Systems XVIII, ed. D. A. Bohlender, D. Durand, & P. Dowler, 251

Martín, S., Mauersberger, R., Martín-Pintado, J., Henkel, C., & García-Burillo, S. 2006, ApJS, 164, 450

Matsushita, S., Trung, D.-V., Boone, F., et al. 2015, ApJ, 799, 26

Meijerink, R., Spaans, M., & Israel, F. P. 2007, A&A, 461, 793

Mills, E. A. C., & Battersby, C. 2017, ApJ, 835, 76

Mills, E. A. C., Güsten, R., Requena-Torres, M. A., & Morris, M. R. 2013, ApJ, 779, 47

Murphy, E. J., Condon, J. J., Schinnerer, E., et al. 2011, ApJ, 737, 67

Nagao, T., Maiolino, R., Marconi, A., & Matsuhara, H. 2011, A&A, 526, A149

Nakai, N., Hayashi, M., Handa, T., et al. 1987, PASJ, 39, 685

Narayanan, D., Cox, T. J., Shirley, Y., et al. 2008, ApJ, 684, 996

Naylor, B. J., Bradford, C. M., Aguirre, J. E., et al. 2010, ApJ, 722, 668

Nguyen-Luong, Q., Nguyen, H. V. V., Motte, F., et al. 2016, ApJ, 833, 23

Nguyen-Q-Rieu, Nakai, N., & Jackson, J. M. 1989, A&A, 220, 57

Olivares E., F., Hamuy, M., Pignata, G., et al. 2010, ApJ, 715, 833

Omont, A. 2007, Reports on Progress in Physics, 70, 1099

Onodera, S., Kuno, N., Tosaki, T., et al. 2010, ApJL, 722, L127

Onus, A., Krumholz, M. R., & Federrath, C. 2018, ArXiv e-prints, arXiv:1801.09952

Origlia, L., Ranalli, P., Comastri, A., & Maiolino, R. 2004, ApJ, 606, 862

Papadopoulos, P. P. 2007, ApJ, 656, 792

Poznanski, D., Butler, N., Filippenko, A. V., et al. 2009, ApJ, 694, 1067

Privon, G. C., Herrero-Illana, R., Evans, A. S., et al. 2015, ApJ, 814, 39

Radburn-Smith, D. J., de Jong, R. S., Seth, A. C., et al. 2011, ApJS, 195, 18

Reiter, M., Shirley, Y. L., Wu, J., et al. 2011, ApJS, 195, 1

Riechers, D. A., Walter, F., Carilli, C. L., et al. 2011, ApJ, 726, 50

Riechers, D. A., Weiß, A., Walter, F., & Wagg, J. 2010, ApJ, 725, 1032

Roberts-Borsani, G. W., Jiménez-Donaire, M. J., Daprà, M., et al. 2017, ApJ, 844, 110

Salak, D., Nakai, N., Miyamoto, Y., Yamauchi, A., & Tsuru, T. G. 2013, PASJ, 65, 66

Sanders, D. B., Mazzarella, J. M., Kim, D.-C., Surace, J. A., & Soifer, B. T. 2003, AJ, 126, 1607

Sandstrom, K. M., Leroy, A. K., Walter, F., et al. 2013, ApJ, 777, 5

Schöier, F. L., van der Tak, F. F. S., van Dishoeck, E. F., & Black, J. H. 2005, A&A, 432, 369

Schruba, A. 2013, in IAU Symposium, Vol. 292, Molecular Gas, Dust, and Star Formation in Galaxies, ed. T. Wong & J. Ott, 311–318

Seaquist, E. R., & Frayer, D. T. 2000, ApJ, 540, 765

Shi, Y., Helou, G., Yan, L., et al. 2011, ApJ, 733, 87

Shi, Y., Yan, L., Armus, L., et al. 2018, ApJ, 853, 149

Shimajiri, Y., André, P., Braine, J., et al. 2017, A&A, 604, A74

Solomon, P. M., Downes, D., Radford, S. J. E., & Barrett, J. W. 1997, ApJ, 478, 144

Solomon, P. M., Radford, S. J. E., & Downes, D. 1992, Nature, 356, 318

Solomon, P. M., & Vanden Bout, P. A. 2005, ARA&A, 43, 677

Sorai, K., Nakai, N., Kuno, N., Nishiyama, K., & Hasegawa, T. 2000, PASJ, 52, 785

Spergel, D. N., Bean, R., Doré, O., et al. 2007, ApJS, 170, 377

Spilker, J. S., Marrone, D. P., Aguirre, J. E., et al. 2014, ApJ, 785, 149

Usero, A., Leroy, A. K., Walter, F., et al. 2015, AJ, 150, 115

Wang, J., Zhang, Z., & Shi, Y. 2011, MNRAS, 416, L21

Warren, B. E., Wilson, C. D., Israel, F. P., et al. 2010, ApJ, 714, 571

Weiß, A., Downes, D., Neri, R., et al. 2007, A&A, 467, 955

Weiß, A., Henkel, C., Downes, D., & Walter, F. 2003, A&A, 409, L41

Weiß, A., Walter, F., & Scoville, N. Z. 2005, A&A, 438, 533

Wild, W., Harris, A. I., Eckart, A., et al. 1992, A&A, 265, 447

Wilson, C. D., Warren, B. E., Israel, F. P., et al. 2012, MNRAS, 424, 3050

Wu, J., Evans, II, N. J., Gao, Y., et al. 2005, ApJL, 635, L173

Wu, J., Evans, II, N. J., Shirley, Y. L., & Knez, C. 2010, ApJS, 188, 313

Wu, P.-F., Tully, R. B., Rizzi, L., et al. 2014, AJ, 148, 7

Yamada, M., Wada, K., & Tomisaka, K. 2007, ApJ, 671, 73

Zhang, Z.-Y., Gao, Y., Henkel, C., et al. 2014, ApJL, 784, L31